MYC uncouples HIF target gene expression from glycolytic flux in hypoxic proliferating primary cells

Courtney A. Copeland[1], Benjamin A. Olenchock[1], David R. Ziehr[1,2], Sarah McGarrity[1,3], Kevin Leahy[1], Jamey D. Young[4], Joseph Loscalzo[1], and William M. Oldham[1,‡]

[1] Department of Medicine, Brigham and Women's Hospital and Harvard Medical School, Boston, MA

[2] Department of Medicine, Massachusetts General Hospital and Harvard Medical School, Boston, MA

[3] Center for Systems Biology, School of Health Sciences, University of Iceland, Reykjavik, Iceland

[4] Departments of Chemical & Biomolecular Engineering and Molecular Physiology & Biophysics, Vanderbilt University, Nashville, TN

[‡] Correspondence: **William M. Oldham <woldham@bwh.harvard.edu>**

Summary

Hypoxia requires metabolic adaptations to sustain cellular functions that underlie numerous physiologic and pathologic processes. While many studies have explored the metabolic consequences of hypoxia in cancer models, comparatively little is known about the metabolic response of primary cells to hypoxia. Here, we performed metabolic flux analyses of proliferating human lung fibroblasts and pulmonary artery smooth muscle cells in hypoxia. Unexpectedly, glycolytic flux was decreased in hypoxic cells despite activation of the hypoxia-inducible factor (HIF) transcriptional program and increased expression of glycolytic enzymes. Pharmacologic activation of HIF with the prolyl hydroxylase (PHD) inhibitor molidustat in normoxia did increase glycolytic flux, but hypoxia abrogated this effect. Multi-omic profiling of cells treated with hypoxia or molidustat, separately or together, revealed distinct molecular responses to hypoxia and pharmacologic PHD inhibition and suggested a critical role for MYC in modulating the HIF response in hypoxia. MYC knockdown in hypoxia increased lactate efflux while MYC overexpression in normoxia blunted the effects of molidustat treatment. Together, these data suggest that other factors, notably MYC, supersede the anticipated effects of HIF-dependent up-regulation of glycolytic gene expression on glycolytic flux in hypoxic proliferating primary cells.

Keywords

hypoxia, metabolic flux analysis, hypoxia-inducible factor, prolyl hydroxylase, metabolism, MYC, pulmonary artery smooth muscle cell, lung fibroblast

30 # Introduction

31 Cellular responses to ambient oxygen levels drive numerous physiologic and pathologic processes from wound
32 healing and angiogenesis to pulmonary vascular remodeling and fibrosis (**Semenza, 2012**). These responses
33 require a sustained capacity for cell proliferation, migration, and protein synthesis, with their associated
34 energetic and metabolic demands, even in the face of limited oxygen availability, or hypoxia. Metazoan cells
35 depend on aerobic respiration to meet cellular energy needs. With an inadequate oxygen supply, cells must
36 reduce energy consumption and shift energy production away from oxidative phosphorylation. Cells accomplish
37 this goal through stabilization of the hypoxia-inducible transcription factor 1α (HIF-1α), which activates the
38 transcription of glucose transporters, glycolytic enzymes, lactate dehydrogenase, and pyruvate dehydrogenase
39 kinase, while decreasing the expression of enzymes in the tricarboxylic acid (TCA) cycle and electron transport
40 chain (**Lee et al., 2020**; **Semenza, 2012**). Although HIF-1α is constitutively expressed, it is hydroxylated by prolyl
41 hydroxylase enzymes (PHDs) in normoxia and targeted for proteasomal degradation. PHDs are the principal
42 oxygen sensors in metazoan cells (**Kaelin and Ratcliffe, 2008**). PHDs are α-ketoglutarate-dependent dioxygenase
43 enzymes that require molecular oxygen for their enzymatic activity. When oxygen tension falls, PHD activity
44 decreases, leading to HIF-1α stabilization and activation of its associated transcriptional program. Overall, the
45 HIF-1 transcriptional program should increase glycolytic capacity and divert glucose-derived pyruvate from
46 oxidative phosphorylation toward lactate fermentation to maintain ATP production and to minimize the
47 formation of reactive oxygen species (ROS) (**Zhang et al., 2008**).

48 While a "glycolytic shift" of primary carbon metabolism in hypoxia is well-described, the effects of hypoxia on
49 other metabolic pathways are an area of active investigation (**Jain et al., 2020**; **Lee et al., 2020**; **Oldham et al.,**
50 **2015**). Since hypoxia is a prominent feature of cancer biology as tumor growth outstrips blood supply, most
51 detailed metabolic studies of cell metabolism in hypoxia have used tumor cell models, yielding important
52 insights into the metabolic pathobiology of cancer (**Garcia-Bermudez et al., 2018**; **Jiang et al., 2016**; **Lee et al.,**
53 **2019**; **Melendez-Rodriguez et al., 2019**; **Metallo et al., 2011**; **Wise et al., 2011**). For example, stable isotope
54 tracing and metabolic flux analyses identified a critical role for reductive carboxylation of glutamine-derived α-
55 ketoglutarate for lipid biosynthesis in supporting tumor growth (**Gameiro et al., 2013**; **Metallo et al., 2011**; **Scott**
56 **et al., 2011**; **Wise et al., 2011**), and metabolomic studies identified aspartate as a limiting metabolite for cancer
57 cell proliferation under hypoxia (**Garcia-Bermudez et al., 2018**). By contrast, comparatively little is known about
58 metabolic adaptations of primary cells to hypoxia and how hypoxic metabolic reprogramming supports
59 homeostasis or promotes pathobiology. Indeed, the importance of reductive carboxylation or aspartate
60 biosynthesis remains to be elucidated in these cells. This and related information would provide an important

61 context for understanding how metabolic reprogramming supports normal cellular responses to hypoxia, how
62 these responses may be (mal)adaptive in a variety of disease contexts, and how the hypoxia metabolic program
63 in primary cells differs from that observed in cancer cells.

64 To address these questions, we have developed models of bioenergetic carbon flux in human lung fibroblasts
65 (LFs) and pulmonary artery smooth muscle cells (PASMCs) cultured in 21% or 0.5% oxygen. These cells were
66 selected as they may be exposed to a wide range of oxygen concentrations *in vivo*, continue to proliferate
67 despite hypoxic culture conditions *in vitro*, and play important roles in the pathology of non-cancerous diseases
68 in which tissue hypoxia is a prominent feature. We found that hypoxia fails to increase glycolysis in these
69 primary cells despite robust up-regulation of the HIF-1 transcriptional program. In normoxia, HIF-1α stabilization
70 by the PHD inhibitor molidustat (BAY-85-3934, "BAY") (**Flamme et al., 2014**) did increase glycolysis and lactate
71 efflux; however, hypoxia blocked this response. These findings suggested the existence of important hypoxia-
72 dependent regulatory mechanisms that override the metabolic consequences of HIF-1-dependent up-regulation
73 of glycolytic gene expression in human primary cells. Transcriptomic profiling suggested a critical role for the
74 transcription factor c-MYC (MYC) in the adaptive response to hypoxia. Using knockdown and overexpression
75 approaches, we demonstrate that MYC attenuates HIF-driven glycolysis in hypoxia and following BAY treatment
76 in these primary cells.

77 Results

78 The goal of this study was to identify the metabolic changes associated with hypoxia in proliferating primary LFs
79 and PASMCs. Cells were seeded and placed into hypoxia for 24 h prior to sample collection to provide adequate
80 time for activation of the hypoxia-dependent transcriptional program. We selected 0.5% oxygen for hypoxia as
81 this level yielded the most reproducible phenotypic differences compared to 21% oxygen culture while being
82 physiologically relevant and above the K_M of cytochrome *c* oxidase (electron transport chain complex IV) for
83 oxygen (**Lee et al., 2020**; **Wenger et al., 2015**). From this starting point, we identified the optimal cell seeding
84 density and time course to capture exponential cell growth (**Figure 1A**), thought to be an indicator of metabolic
85 steady state. LFs cultured in 0.5% oxygen grew slower than LFs cultured in 21% oxygen (**Figure 1B**), but slower
86 growth was not associated with decreased cell viability (**Figure S1A**). These cells demonstrated robust
87 stabilization of HIF-1α protein associated with up-regulation of downstream targets, such as glucose transporter
88 1 (GLUT1) and lactate dehydrogenase A (LDHA) (**Figures 1K, E-H**). These changes persisted for the duration of
89 the experimental time course.

Extracellular flux analysis reveals little impact of hypoxia on glycolysis

Having established a model system, we next determined the extracellular fluxes of glucose (GLC), lactate (LAC), pyruvate (PYR), and amino acids (**Figures 1I-J**). Flux calculations incorporated changes in cell number, extracellular metabolite concentrations, and medium evaporation over time (**Murphy and Young, 2013**) (**Figure S1**). Surprisingly, we observed no significant differences in glucose uptake or lactate efflux rates in 0.5% oxygen cultures (**Figure 1I**) despite activation of the HIF-1 transcriptional program as reflected by increased expression of GLUT1 and LDHA. No change in glucose or lactate fluxes were observed when the ambient oxygen level was decreased further to 0.2% (**Figure S2**). Similar results were also observed in PASMCs where lactate efflux was significantly *decreased* by 0.5% ambient oxygen (**Figure S3**).

In addition to glucose and lactate, we also determined the extracellular fluxes of pyruvate and amino acids. Overall, changes were modest, with hypoxia generally decreasing the fluxes of all measured metabolites. Notably, a substantial decrease in glutamine consumption was observed in LFs cultured in 0.5% oxygen. This observation is in contrast to previous studies in cancer cell metabolism demonstrating increased glutamine uptake as a key feature of the metabolic response to hypoxia (**Gameiro et al., 2013**; **Metallo et al., 2011**; **Wise et al., 2011**). Similar patterns were observed in 0.2% oxygen (**Figure S2**). In PASMCs, glutamine uptake did increase, as did the uptake of branched-chain amino acids and arginine (**Figure S3**), highlighting differential responses of these mesenchymal cells to hypoxia.

Given that hypoxia did not increase glucose and lactate fluxes as expected based on the observed increases in glycolytic gene expression, we next assessed the capacity of HIF-1α to augment glycolysis in LFs. Cells were treated with the prolyl hydroxylase inhibitor BAY to stabilize HIF-1α under 21% oxygen conditions (**Figure 1**). Similar to hypoxia, BAY decreased cell growth rate (**Figures 1A-B**) and activated the HIF-1 transcriptional program (**Figures 1D-H**). Compared to hypoxia, BAY treatment resulted in a similar activation of HIF-1 target gene transcription and protein expression. In normoxia, this transcriptional program was associated with substantially increased glucose uptake and lactate efflux (**Figure 1I**). Comparatively modest effects of BAY on amino acid fluxes were observed as compared to 0.5% oxygen culture conditions (**Figure 1J**) with preservation of glutamine uptake, alanine efflux, and glutamate efflux rates.

Stable isotope labeling suggests limited metabolic reprogramming in hypoxia

To validate the findings from our extracellular flux measurements, we next treated LFs with stable carbon isotopes of glucose and glutamine to measure the rate and trace the incorporation of ^{13}C into key downstream

119 carbon utilization pathways (**Figures 2, S4-S5**). Consistent with our extracellular flux measurements, we found
120 that the rate of label incorporation from [U-$^{13}C_6$] glucose into pyruvate was similar across 21%, 0.5%, and DMSO-
121 treated conditions, but markedly increased with BAY treatment (**Figures 2A-B**).

122 Several patterns of isotope labeling emerge across the treatment conditions (**Figures 2C, S4**). For the glycolytic
123 intermediates fructose bisphosphate (FBP), 3-phosphoglycerate (3PG), and pyruvate (PYR), label incorporation
124 from the glucose tracers is decreased with hypoxia and BAY treatments (*i.e.*, the unlabeled, or M0, fraction was
125 greater). This is also true for the tricarboxylic acid cycle (TCA) metabolites citrate (CIT), α-ketoglutarate (AKG),
126 and malate (MAL) labeled with [1,2- $^{13}C_2$ glucose]. By contrast, these metabolites show increased labeling with
127 [U-$^{13}C_6$] glucose. The citrate labeling pattern indicates increased label incorporation into M3 and M5 isotopes,
128 reflecting carbon entry through pyruvate carboxylase, which catalyzes the carboxylation of pyruvate to
129 oxaloacetate. The [U-$^{13}C_5$] glutamine label was not incorporated into pyruvate or upstream glycolytic
130 intermediates. The labeling of TCA metabolites by glutamine was decreased in hypoxia and BAY treatment with
131 a more pronounced effect of BAY treatment. Compared to previous studies of metabolic flux in cancer cells
132 (**Metallo et al., 2011**; **Wise et al., 2011**), no marked increase in M5-labeled citrate from [U-$^{13}C_5$] glutamine was
133 observed with hypoxia treatment, suggesting no change in reductive carboxylation for lipid synthesis in LFs. The
134 overall fraction of M5-citrate in these cells was low (< 7%).

135 The stable isotope labeling patterns in PASMCs were similar to LFs (**Figure S5**) where labeling was attenuated in
136 hypoxia. The most notable differences between LF and PASMC labeling were observed in citrate. Compared with
137 LFs, PASMCs demonstrated a marked reduction of M2-citrate labeled by glucose and no change in the labeling of
138 M3-citrate by [U-$^{13}C_6$] glucose. These data suggest decreased glucose entry into the TCA cycle *via* pyruvate
139 dehydrogenase and no change in the activity of pyruvate carboxylase, respectively. Interestingly, unlike LFs,
140 PASMCs demonstrated increased production of M5-citrate from [U-$^{13}C_5$] glutamine in hypoxia (7.91% ± 0.89% *v*.
141 18.24% ± 2.67%, $p = 0.04$) consistent with increased reductive carboxylation in support of lipid synthesis in these
142 cells, similar to prior observations in cancer cells, but distinct from LFs studied here.

143 Glycolytic flux in hypoxia is closely coupled to cell growth rate

144 The mass isotopomer distribution for a given metabolite is determined based on a complicated relationship
145 among the rate of isotope incorporation into the metabolic network, the contributions of unlabeled substrates,
146 and fluxes through related pathways. To clarify how these labeling patterns reflect changes in intracellular
147 metabolite fluxes, we next generated metabolic flux models incorporating the extracellular flux measurements
148 and stable isotope tracing data described above. Preliminary labeling time courses indicated that, even after 72

149 h of labeling, intracellular metabolites did not reach isotopic steady state (**Figure S6**). Thus, we performed
150 isotopically non-stationary metabolic flux analysis as implemented by Isotopomer Network Compartment
151 Analysis (INCA) (**Jazmin and Young, 2013**; **Murphy et al., 2013**; **Young, 2014**) (**Figures 3, S7, Tables S1-S3**).
152 Overall, proliferating LFs demonstrated high rates of glucose uptake and glycolysis. Approximately 10% of
153 cytoplasmic pyruvate enters the TCA cycle with the balance converted to lactate (**Figure S7A**). Consistent with
154 extracellular flux measurements and isotope labeling patterns described above, significant reductions in
155 glycolysis, the TCA cycle, and amino acid metabolism were observed in the metabolic flux models of LFs cultured
156 in hypoxia. A significant increase in pentose phosphate pathway flux was also observed, although the absolute
157 flux through this pathway is low (**Figure 3A**). By contrast, HIF-1 activation by BAY in 21% oxygen increased
158 glycolysis and lactate fermentation by ~50% (**Figure 3B**), but had a similar effect as hypoxia in decreasing serine
159 and glutamine incorporation. Metabolite fluxes in DMSO-treated cells were similar to 21% oxygen controls.

160 In normoxia, the magnitude of intracellular metabolite fluxes was generally similar in LFs and PASMCs (**Figures**
161 **S7A, S7B, Tables S1, S3**). LFs had greater consumption of serine while PASMCs had greater efflux of alanine. In
162 hypoxia, PASMCs exhibited similar decreases in glycolytic flux as LFs but also a marked, and unexpected,
163 increase in TCA flux (**Figure S7C**). The increased TCA flux in PASMCs was driven by increased glutamine
164 consumption in these cells. This finding is similar to a prior report of glutamine-driven oxidative phosphorylation
165 in hypoxic cancer cells (**Fan et al., 2013**), although glycolysis was also up-regulated in the hypoxia-exposed
166 cancer cells studied in this report.

167 Given the global decrease in bioenergetic metabolic flux in hypoxic LFs, we hypothesized that these differences
168 may be a consequence of decreased growth rate. After normalizing metabolite fluxes in normoxia and hypoxia
169 to the cell growth rate, modest increases (~10%) in glycolytic flux were observed (**Figure S7D**). This finding
170 suggests that, while glycolysis increases relative to growth rate in hypoxic cells, the regulators of cell
171 proliferation rate override the consequences of the HIF-1 transcriptional program. Indeed, even after adjusting
172 for cell growth rate, the relative increase in glycolytic flux is modest compared to the marked up-regulation of
173 glycolytic protein levels. BAY treatment decreased cell proliferation rate (**Figure 1B**), indicating that, unlike
174 hypoxia, BAY treatment in normoxia uncouples cell proliferation and metabolic flux.

175 Hypoxia and BAY treatment increase lactate oxidation

176 Although the metabolite exchange fluxes for bidirectional reactions tend to be poorly resolved, two
177 observations are worth highlighting (**Tables S1-S3**). First, consistent with the stable isotope tracing results, the
178 modeled rate of reductive carboxylation through reverse flux by isocitrate dehydrogenase in LFs is low (~4

179 fmol/cell/h), unchanged by hypoxia, and modestly increased by BAY treatment. By contrast, the rate of
180 reductive carboxylation increases 6-fold in PASMCs in hypoxia, highlighting an important role for this pathway in
181 the metabolic response of these cells to hypoxia.

182 Second, PHD inhibition is associated with a marked increase in the lactate transport exchange flux in LFs from ~
183 0 to 1,500 and 700 fmol/cell/h in 0.5% oxygen and BAY treatment conditions, respectively, with similar results in
184 PASMCs. Since the net lactate transport flux is secretion, this observation suggests increased lactate uptake with
185 hypoxia or BAY treatment. This finding may be consistent with the HIF-driven increased expression of the
186 reversible lactate transporter MCT4 (**Contreras-Baeza et al., 2019**). To investigate this hypothesis, LFs and
187 PASMCs were treated with [U-$^{13}C_3$] lactate (2 mM) and ^{13}C incorporation into intracellular metabolites was
188 analyzed by LC-MS (**Figures 4, S5**). Notably, lactate labeled ~50% of citrate and ~20% of downstream TCA cycle
189 metabolites in both LFs and PASMCs, indicating that lactate may be an important respiratory fuel source in these
190 cells even though lactate efflux is high. Although lactate has been used less commonly than glucose and
191 glutamine in stable isotope tracing studies, Faubert and colleagues (**2013**) demonstrated lactate incorporation in
192 human lung adenocarcinoma *in vivo*. In this study, lactate incorporation corresponded to regions of high glucose
193 uptake as determined by [^{18}F]-fluorodeoxyglucose positron emission tomography, suggesting that lactate
194 consumption can occur in areas of high glucose utilization. Subsequently, investigators have demonstrated the
195 importance of lactate as a metabolic fuel *in vivo* (**Hui et al., 2017a**, **2020**). With hypoxia or BAY treatment, we
196 observed increased labeling of the TCA metabolites citrate (CIT), α-ketoglutarate (AKG), malate (MAL), and
197 aspartate (ASP) in LFs. Interestingly, although increased labeling of pyruvate was observed in hypoxic PASMCs,
198 the label was not incorporated into the TCA cycle as observed in LFs (**Figure S5**).

199 In addition to downstream metabolites, we also observed hypoxia- and BAY-dependent increases in lactate
200 incorporation in fructose bisphosphate (FBP) and 3-phosphoglycerate (3PG). This observation is consistent with
201 prior reports describing hypoxia-mediated increases in glycogen synthesis (**Favaro et al., 2012**; **Pelletier et al.,**
202 **2012**; **Pescador et al., 2010**). Together, these data suggest that lactate also makes a small (~5% carbon)
203 contribution to glycogen precursors.

204 Hypoxia abrogates the effects of BAY on increasing glycolysis

205 To reconcile the differential effects of prolyl hydroxylase inhibition by hypoxia and BAY, we next addressed
206 whether hypoxia could suppress the effects of BAY on glucose and lactate fluxes (**Figures 5A-C**). LFs cultured in
207 standard growth medium were treated with BAY and placed in either 21% or 0.5% oxygen. Similar to previous
208 experiments, BAY treatment decreased cell growth rate, increased glucose uptake, and increased lactate efflux

209 in 21% oxygen. Interestingly, when combined with 0.5% oxygen, BAY treatment was unable to enhance lactate
210 efflux. These data suggest that hypoxia antagonizes the effects of HIF-1 activation on glycolytic flux in these
211 primary cells.

212 To investigate these metabolic differences further, we performed metabolomic profiling of LFs treated for 72 h
213 with hypoxia or BAY separately or in combination (**Figures 5D-F**). Both 0.5% oxygen and BAY treatment induced
214 marked changes in intracellular metabolite levels (**Figure S8**). Of 133 metabolites, 98 were differentially
215 regulated by hypoxia and 54 were differentially regulated by BAY. Of the differentially regulated metabolites, 44
216 were affected by both 0.5% oxygen and BAY treatment (**Figure S8C**). Metabolite set enrichment analysis of KEGG
217 biochemical pathways was consistent with the results of the metabolic models demonstrating significant
218 enrichment of the pentose phosphate pathway with 0.5% oxygen or BAY treatment; decreased alanine,
219 aspartate, and glutamate metabolism with hypoxia; and increased glycolysis/gluconeogenesis with BAY (**Figures**
220 **S8D, S8E**). Indeed, aspartate was the most significantly decreased metabolite with both treatments, consistent
221 with prior reports demonstrating an important role for HIF-1 regulation of aspartate biosynthesis in cancer cells
222 (**Garcia-Bermudez et al., 2018**; **Melendez-Rodriguez et al., 2019**).

223 Principal component analysis revealed greater class similarity among both treatment groups cultured in 0.5%
224 oxygen than among the BAY-treatment groups (**Figure 5D**). Moreover, these hypoxia-treated cells were well-
225 segregated from BAY-treated cells. These observations are, again, consistent with the results of the metabolic
226 flux models demonstrating an overriding effect of hypoxia *per se* on metabolic flux and highlighting important
227 differences between hypoxic and pharmacologic PHD inhibition. To identify the key differences among these
228 treatments, we performed linear modeling focusing on those metabolites with a significant interaction term in
229 the model described by treatment × oxygen (**Figure 5E**) (*i.e.*, metabolites where the change with hypoxia
230 treatment was different from the change with BAY treatment). Of 133 metabolites, 77 were significantly
231 differentially regulated by hypoxia and BAY treatments. Several patterns emerged from this analysis (**Figure 5F**).
232 Interestingly, the hypoxia-regulated metabolite, 2-hydroxyglutarate (**Oldham et al., 2015**), increased following
233 BAY treatment, but was unaffected by hypoxia treatment in proliferating LFs. The tricarboxylic acid (TCA) cycle
234 metabolite aconitate was decreased in hypoxia, but increased by BAY treatment, while the opposite effect was
235 observed for hydroxyproline and taurine. The glycolytic intermediate glyceraldehyde 3-phosphate (GAP) was
236 decreased by both hypoxia and BAY, while hypoxia reversed the BAY-mediated decrease in γ-aminobutyric acid
237 (GABA). A metabolite set enrichment analysis of these differentially regulated metabolites revealed the TCA
238 cycle to be the most enriched KEGG metabolite set (**Figure 5G**). Leading edge analysis demonstrated negative
239 enrichment scores associated with all of the TCA metabolites detected by our platform (**Figure 5H**). This result

240 indicates a more modest impact of BAY treatment on the TCA cycle than hypoxia, as suggested by our metabolic
241 flux models where hypoxia resulted in a 1.5-2-fold reduction of TCA flux compared to a 1.1-1.5-fold reduction
242 with BAY treatment in normoxia (**Figure 3**).

243 In addition to these differential effects on polar metabolite levels, perhaps the most significant contrast
244 between hypoxia and BAY treatment is the impact of hypoxia on cellular redox state. As oxygen deprivation
245 causes reductive stress (**Xiao and Loscalzo, 2020**), we next measured the impact of these treatments on
246 intracellular NAD(H) as a surrogate for cellular redox state (**Figures 5I-K**). As expected, hypoxia increased the
247 $NADH/NAD^+$ ratio, driven primarily by a decrease in intracellular NAD^+. Interestingly, while BAY treatment
248 increased the levels of NADH, a concomitant increase in NAD^+ resulted in preservation of the $NADH/NAD^+$ ratio.
249 As NADH accumulation is a putative inhibitor of glycolytic flux (**Tilton et al., 1991**), this may be one mechanism
250 by which glycolytic flux is decreased in hypoxia but not following BAY treatment.

251 Transcriptomic analysis identifies regulators of metabolism in hypoxia

252 To identify the upstream regulators of the observed metabolic changes, we next performed transcriptomic
253 analysis of LFs treated with hypoxia or BAY, separately or together (**Figure 6, S9**). As anticipated, both hypoxia
254 and BAY treatment induced substantial changes in gene expression (**Figure S9A, S9B**). Of the 7,789 differentially
255 expressed genes across both conditions, 891 (11%) were unique to BAY treatment in normoxia, 1,649 (21%)
256 were shared between BAY and hypoxia, while 5,249 (67%) were unique to 0.5% hypoxia culture (**Figure S9C**).
257 Gene set enrichment analysis of these differentially regulated metabolites was performed using Molecular
258 Signatures Database "Hallmark" gene sets (**Liberzon et al., 2015**) (**Figures S9D, S9E, S9F**). As expected, both
259 treatments were associated with enrichment of the "hypoxia" and "glycolysis" gene sets.

260 Given the disparate effects of hypoxic and pharmacologic PHD inhibition on cellular metabolism described
261 above, we focused our transcriptomics analyses on the differences between hypoxia and BAY treatments.
262 Principal component analysis again demonstrates clear separation among the four treatment groups (**Figure 6A**).
263 The first and second principal components correspond to 0.5% oxygen and BAY treatments, respectively.
264 Consistent with our prior observations, the combination of 0.5% oxygen plus BAY was more similar to 0.5%
265 oxygen alone with decreased distance between both hypoxia-treated groups along the axis of the second
266 principal component, again, consistent with the hypothesis that hypoxia uncouples the effects of BAY treatment.
267 To identify those transcripts that were differentially affected by hypoxia compared to BAY treatment alone, we
268 performed linear modeling to identify transcripts with a significant interaction term in the model described by
269 treatment × oxygen (**Figure 6B**). With this analysis, we found several patterns of transcriptional changes (**Figure**

270 **6C**). For example, EPAS1, the gene encoding the HIF-2α protein, was markedly decreased by hypoxia, compared
271 to its modest reduction following BAY treatment. A similar, but opposite, effect on RBM3 (RNA-binding protein
272 3) expression was observed. RBM3 supports the viability and proliferation of neural stem cells in hypoxia (**Yan et**
273 **al., 2019**). Histone deacetylase 9 (HDAC9) and prolyl 4-hydroxylase subunit α2 (P4HA2) demonstrated opposing
274 effects following hypoxia and BAY treatment, where BAY decreased HDAC9 expression and increased P4HA2
275 expression. Together, this subset of transcriptional changes illustrates important differences between hypoxia
276 and HIF stabilization in normoxia.

277 Interestingly, an enrichment analysis of transcripts differentially regulated by 0.5% oxygen and BAY treatment
278 actually demonstrated greater enrichment of the "hypoxia" gene set following BAY treatment alone than with
279 hypoxia itself (**Figure 6D**). Similarly, the gene set for glycolysis was also more enriched following BAY treatment
280 than hypoxia treatment. The most enriched gene sets associated with hypoxia included pro-proliferative "E2F
281 targets" and "G2/M checkpoint" proteins as well as "MYC targets." These findings were further supported by a
282 transcription factor enrichment analysis identifying enrichment of MYC target proteins associated with hypoxia
283 (**Figure 6E**).

284 MYC antagonizes HIF-dependent glycolytic fluxes

285 Consistent with our bioinformatic results, immunoblotting demonstrated increased MYC protein levels in
286 hypoxia-treated cells, but not with BAY-treatment alone, where MYC was decreased (**Figure 7A-B**). To test the
287 hypothesis that hypoxia-induced MYC expression inhibits glycolysis in hypoxic primary cells, we first combined
288 MYC knockdown with hypoxia treatment (**Figure 7C-E**). As expected, MYC-deficient cells proliferated more
289 slowly in normoxia and MYC was absolutely essential for sustaining cell proliferation in hypoxia (**Figure 7D**).
290 Consistent with our hypothesis, MYC knockdown cells demonstrated increased lactate efflux upon hypoxia
291 treatment, unlike control siRNA-treated cells (**Figure 7E**). We next performed the complementary experiment to
292 determine whether MYC overexpression could attenuate the increase in glycolysis observed with BAY treatment
293 (**Figure 7F-H**). MYC increased the proliferation rate of DMSO-treated cells, although it did not augment the
294 proliferation rate of BAY-treated cells. As expected, MYC overexpression blocked the BAY-stimulated increase in
295 lactate efflux. Together, these data suggest that hypoxia-induced MYC expression may be one factor that
296 uncouples the HIF transcriptional program from glycolytic flux in proliferating primary cells.

297 # Discussion

298 In this work, we used ^{13}C metabolic flux analysis to identify hypoxia-mediated metabolic changes in proliferating
299 human primary cells. Our principal finding was that hypoxia reduced, rather than increased, carbon flux through
300 glycolysis and lactate fermentation pathways despite robust activation of the HIF transcriptional program and
301 up-regulation of glycolytic genes. Certainly, the LFs studied here are capable of augmenting glycolysis in
302 response to HIF stabilization, as demonstrated by experiments with the PHD inhibitor BAY; however, these
303 effects are completely attenuated when BAY-treated cells are cultured in hypoxia. Together, these findings
304 suggest that changes in enzyme levels alone are insufficient to alter metabolic flux in hypoxia and point to the
305 importance of regulatory mechanisms that supersede the effects of HIF-dependent gene transcription in primary
306 cells.

307 Our data indicate that hypoxia-induced MYC expression is one such regulatory mechanism. MYC is a
308 transcription factor that regulates the expression of numerous genes involved in many biological processes,
309 including metabolism, proliferation, apoptosis, and differentiation (**Dang et al., 2006**; **Li et al., 2020**; **Stine et al.,**
310 **2015**). As deregulated MYC activity has been associated with the majority of human cancers (**Vita and**
311 **Henriksson, 2006**), much of our understanding of MYC regulation comes from studies using cancer cell models
312 (**Dang, 2012**; **Li et al., 2020**; **Madden et al., 2021**; **Stine et al., 2015**), while the role of MYC in the biology of
313 untransformed cells is less well understood. The literature describes a complex and reciprocal relationship
314 between HIF and MYC that depends on both environmental (*e.g.*, hypoxia) and cellular context (**Li et al., 2020**).
315 Generally, HIF-1 has been observed to inhibit MYC through multiple mechanisms [koshiji2004; koshiji2005;
316 **Gordan et al.** (**2007**); **Zhang et al.** (**2007**)], and this previous work is consistent with our observations that HIF
317 stabilization following BAY treatment decreased MYC protein and target gene expression. Conversely, MYC has
318 been implicated in increased HIF activity through transcriptional and post-transcriptional mechanisms (**Chen et**
319 **al., 2013**; **Doe et al., 2012**; **Zhang et al., 2009**), primarily in the context of malignant transformation. The
320 observation that MYC may antagonize the transcriptional effects of HIF to sustain primarily cell proliferation and
321 metabolism in hypoxia suggests a substantially different regulatory relationship than has been previously
322 described.

323 Understanding how MYC transcriptional activity affects hypoxic primary cell metabolism is imperative to our
324 understanding of cellular adaptation to hypoxia. MYC stimulates the expression of nuclear-encoded
325 mitochondrial genes and promotes mitochondrial biogenesis, both directly and through activation of
326 mitochondrial transcriptional factor A (TFAM) (**Li et al., 2005**). Indeed, we found that the oxidative

327 phosphorylation gene set was relatively enriched with hypoxia treatment compared to BAY treatment (**Figure**
328 **6D**). In this way, hypoxic MYC activation may sustain energy production by oxidative phosphorylation, thereby
329 decreasing the energetic demands driving increased glycolytic flux. Beyond oxidative phosphorylation, MYC
330 targets genes involved in many other intermediary metabolic pathways, including amino acids, nucleotides, and
331 lipids (**Stine et al., 2015**), that may also impact the central pathways of carbon metabolism studied in this work.

332 Beyond MYC, the identification of other HIF-independent mechanisms regulating primary cell adaption to
333 hypoxia is of critical importance. Cells express several oxygen-dependent enzymes in addition to PHD whose
334 activities may be altered in hypoxia but not by PHD inhibition. For example, PHD is one of many α-ketoglutarate-
335 dependent dioxygenase enzymes that rely on molecular oxygen for their catalytic activity (**Islam et al., 2018**).
336 Jumonji-C (JmjC) domain-containing histone demethylases are other prominent members of this family whose
337 inhibition by hypoxia has been shown to cause rapid and HIF-independent induction of histone methylation
338 (**Batie et al., 2019**). Indeed, our transcription factor enrichment analysis (**Figure 6E**) demonstrates that this
339 family of lysine demethylases (KDMs) was the most enriched with 0.5% oxygen treatment as compared to BAY
340 treatment. Similarly, a recently described cysteamine dioxygenase has been shown to mediate the oxygen-
341 dependent degradation of Regulators of G protein Signaling 4 and 5 and IL-32 (**Masson et al., 2019**). In addition
342 to dioxygenase enzymes, electron transport chain dysfunction resulting from impaired Complex IV activity leads
343 to increased ROS production in hypoxia (**Chandel et al., 1998**). Mitochondrial ROS increase the half-lives of
344 several mRNAs in hypoxia, including MYC, as we observed in this work, independent of HIF stabilization (**Guzy et**
345 **al., 2005**). Finally, hypoxia imposes a reductive stress on cells associated with an increase in the $NADH/NAD^+$
346 ratio secondary to impaired electron transport (**Figure S5K**) (**Chance and Williams, 1955**; **Garofalo et al., 1988**).
347 NADH accumulation may slow glycolysis *via* feedback inhibition of GAPDH (**Tilton et al., 1991**). Any or all of
348 these molecular mechanisms may also contribute to uncoupling glycolytic enzyme expression from glycolytic
349 flux as observed in the experiments described here.

350 In addition to its effects on cellular metabolism, another canonical role of HIF-1 activation is slowing of cellular
351 proliferation rate in the face of limited oxygen availability (**Hubbi and Semenza, 2015**), which is precisely what
352 we observed here (**Figures 1B, 5A**). The effects of HIF-1 on cell proliferation rate are mediated, in part, by
353 increased expression of cyclin-dependent kinase inhibitor p21 (*CDKN1A*), inhibition of E2F targets (**Gardner et**
354 **al., 2001**), and inhibition of pro-proliferative MYC signaling (**Koshiji et al., 2004**). These transcriptional effects are
355 precisely what is observed in BAY treated LFs in normoxia. By contrast, hypoxia culture was associated with
356 decreased expression of p21, consistent with a previous report (**Mizuno et al., 2009**), as well as increased
357 expression of MYC protein and enrichment of MYC target genes. Indeed, the most marked differences between

358 hypoxia and BAY treatment on LF gene transcription were the up-regulation of pro-proliferative gene sets
359 containing E2F targets and G2/M checkpoint proteins. Much of this transcriptional response may be mediated
360 by hypoxia-induced up-regulation of MYC, which is known to stimulate cell cycle progression through its effects
361 on the expression and activity of cyclins, cyclin-dependent kinases, and cyclin-dependent kinase inhibitors
362 (**Hydbring et al., 2017**). Clarifying the complex interactions among HIFs, MYC, and cell proliferation will be
363 important for understanding the cellular response of these mesenchymal cells to tissue injury.

364 Taken together, these findings raise important questions regarding the cell-autonomous role of HIFs in the
365 hypoxia response. On an organismal level, HIFs drive expression of angiogenic and erythropoietic factors to
366 increase oxygen delivery to hypoxic tissues. Within individual cells, HIF-1α seems to be important for mitigating
367 the adverse effects of ROS formation by dysfunctional electron transport in the mitochondria. Indeed, hypoxia
368 increased oxygen consumption and ROS production in HIF-1α-null mouse embryonic fibroblasts (MEFs), which
369 was associated with increased cell death (**Zhang et al., 2008**). Interestingly, these cells also had increased ATP
370 levels compared to wild type, suggesting that mitochondrial function was adequate under 1% oxygen culture
371 conditions to support oxidative phosphorylation and meet the energy needs of the cells. Given the prominence
372 of HIFs in mediating the transcriptional response to hypoxia, it is somewhat surprising that neither PHD, HIFs,
373 nor their downstream targets were found to be selectively essential as a function of oxygen tension in a
374 genome-wide CRISPR growth screen of K562 human lymphoblasts cultured in normoxia or hypoxia (**Jain et al.,**
375 **2020**). Similarly, knockout of HIF signaling did not affect growth, internal metabolite concentrations, glucose
376 consumption, or lactate production under hypoxia by human acute myeloid leukemia cells (**Wierenga et al.,**
377 **2019**). Together with our results, these studies highlight the need for additional research linking hypoxia-
378 induced metabolic changes to their transcriptional and post-transcriptional regulatory mechanisms, particularly
379 in primary cells.

380 This work also highlights two specific metabolic features that appear to be important in the metabolic response
381 of these primary cells to hypoxia. First, both LFs and PASMCs demonstrated notable incorporation of lactate-
382 derived carbon into intracellular metabolic pathways that increased with hypoxia and BAY treatments (**Figures 4,**
383 **S5**). This finding is consistent with increasing evidence suggesting an important role for lactate as a metabolic
384 fuel in several organ systems (**Faubert et al., 2013**; **Hui et al., 2017b**). Although typically considered a metabolic
385 waste product (**Rabinowitz and Enerback, 2020**), an important contribution of lactate *import* in supporting
386 metabolic homeostasis in the face of an ischemic insult, which is associated with increased extracellular lactate,
387 is an evolutionarily attractive hypothesis that merits further investigation. Second, PASMCs, but not LFs,
388 demonstrated significant rates of reductive carboxylation that increased in 0.5% oxygen (**Figure S5**). Reductive

389 carboxylation was first identified in hypoxic tumor cells where stable isotope tracing revealed ^{13}C incorporation
390 from labeled glutamine into lipids (**Gameiro et al., 2013**; **Metallo et al., 2011**; **Scott et al., 2011**; **Wise et al.,**
391 **2011**). Hypoxia drives PASMC proliferation *in vivo* contributing to the development pulmonary hypertension in
392 humans and animal models. Isocitrate dehydrogenase has previously been implicated in the pathobiology of this
393 disease (**Fessel et al., 2012**), and our findings suggest that reductive carboxylation catalyzed by isocitrate
394 dehydrogenase may be a metabolic vulnerability of hypoxic PASMCs associated with pulmonary vascular
395 disease.

396 Our finding that hypoxia was associated with decreased glycolysis and lactate fermentation was unexpected.
397 Several aspects of our experimental design may have contributed to this finding. First, our goal was to
398 understand how metabolic reprogramming may support cell proliferation in hypoxia. Thus, we measured
399 metabolite fluxes in cells during the exponential growth phase accounting for cell growth rate, metabolite
400 degradation rates, and medium evaporation with multiple measurements over a 72 h time course. Often, cells
401 are studied near confluence, where metabolic contributions to biomass production are less and the rate of
402 glycolysis in hypoxia may be higher. Second, we began our experimental treatments 24 h prior to collecting
403 samples to ensure that the hypoxia metabolic program was established prior to labeling. Similar studies
404 (**Grassian et al., 2014**; **Metallo et al., 2011**) typically placed cells into hypoxia at the time of labeling. Third, and
405 perhaps most importantly, these flux determinations were performed in human primary cell cultures rather than
406 immortalized cell lines. Although both cell types used in this study were derived from lung, we anticipate that
407 many of our findings will be generalizable to primary cells from different tissues.

408 In summary, in this metabolic flux analysis of proliferating human primary cells *in vitro*, we have demonstrated
409 that MYC uncouples an increase in HIF-dependent glycolytic gene transcription from glycolytic flux in hypoxia.
410 Indeed, the degree of metabolic reprogramming in hypoxia was modest and suggests close coupling between
411 proliferation and metabolism. In light of our findings, additional studies are warranted to clarify the role of HIFs
412 in mediating the metabolic response to hypoxia, to determine how MYC activity is regulated by hypoxia, and to
413 identify other key regulators of hypoxic metabolic reprogramming in primary cells. Moreover, these data
414 strongly caution investigators against drawing conclusions about metabolite flux from measures of gene
415 transcription alone.

416

Acknowledgements

This work was supported by grants from the NIH (K08HL128802), American Lung Association, Pulmonary Hypertension Association, and the American Thoracic Society Foundation to W.M.O and from the NIH (U01HG007690, U54HL119145, R01HL155107, R01HL155096) and the American Heart Association (D700382, CV-19) to J.L.

Author Contributions

W.M.O. conceived and designed the analysis. C.A.C., B.A.O., D.R.Z., S.M., K.L., and W.M.O. collected the data. J.D.Y. and W.M.O. contributed data or analysis tools. W.M.O. performed the analysis. W.M.O. drafted the manuscript. All authors participated in interpreting the results and revising the manuscript. All authors approve the final submission.

Declaration of Interests

The authors declare no competing interests.

430 # Figure Legends

431 Figure 1: **Effects of prolyl hydroxylase inhibition on extracellular metabolite fluxes in lung fibroblasts.** Lung
432 fibroblasts (LFs) were cultured with 21% oxygen (*red*), 0.5% oxygen (*blue*), DMSO (0.1% v/v, *green*), or
433 molidustat (BAY, 10 µM, *purple*) beginning 24 h prior to time 0. (**A**) Growth curves of LFs in each experimental
434 condition (n = 8). (**B**) Growth rates from (A) were determined by robust linear modeling of log-transformed
435 growth curves. (**C**, **D**) Representative immunoblots of LF protein lysates cultured as in (A). (**E**, **F**) Relative change
436 in HIF-1α (E) and LDHA (F) protein levels normalized to 21% oxygen or DMSO treatment time 0 (n = 4). (**G**, **H**)
437 Relative changes in GLUT1 (G) and LDHA (H) mRNA levels normalized to 21% oxygen or DMSO treatment time 0
438 (n = 4). (**I**, **J**) Extracellular fluxes of the indicated metabolites (n = 8). Data are mean ± SEM. Comparisons were
439 made using linear mixed effects models with treatment group as a fixed effect and biological replicate as a
440 random effect. Tukey's *post hoc* test was applied to determine differences between 21% and 0.5% oxygen (*),
441 between DMSO and BAY treatment (†), or between 0.5% oxygen and BAY treatment (‡) with adjusted p-values <
442 0.05 considered significant.

443 Figure 2: **Stable isotope tracing of lung fibroblasts.** (**A**) Fraction of pyruvate labeling following treatment of lung
444 fibroblasts (LFs) with [U-$^{13}C_6$] glucose. (**B**) Rate values determined from asymptotic regression fit of the data
445 from (A). (**C**) Isotopic labeling of key intracellular metabolites after 72 h of treatment with the indicated tracers.
446 Experimentally determined mass isotope distributions were corrected for natural isotope abundance. Data are
447 the mean ± SEM of 4 biological replicates. Significant differences in labeling patterns between 21% and 0.5%
448 oxygen (*), DMSO and BAY treatment (†), and 0.5% oxygen and BAY treatment (‡) for each combination of
449 metabolite and tracer are highlighted. FBP, fructose bisphosphate; 3PG, 3-phosphoglycerate; AKG, α-
450 ketoglutarate.

451 Figure 3: **Metabolic flux maps of lung fibroblasts.** (**A**) Ratio of metabolic fluxes in 0.5% oxygen compared to 21%
452 oxygen. (**B**) Ratio of metabolic fluxes in cells treated with molidustat (BAY) compared to DMSO vehicle control.
453 Fluxes with non-overlapping confidence intervals are highlighted with colored arrows to indicate significant
454 changes. Arrow thickness corresponds to absolute flux in hypoxia- or BAY-treated cells.

455 Figure 4: **PHD inhibition increases lactate uptake and oxidation.** Mass isotopomer distributions of key
456 metabolites following labeling with [U-$^{13}C_3$] lactate (2 mM) for 72 h indicates increased lactate uptake and
457 oxidation in hypoxia or with molidustat (BAY) treatment. Data are mean ± SEM of n = 4 biological replicates.
458 Comparisons were made using linear mixed effects models with treatment group as a fixed effect and biological
459 replicate as a random effect. Tukey's *post hoc* test was applied to determine differences between 21% and 0.5%

460 oxygen (*), between DMSO and BAY treatment (†), or between 0.5% oxygen and BAY treatment (‡) with
461 adjusted p-values < 0.05 considered significant.

462 Figure 5: **Metabolomic analysis of molidustat treatment in normoxia and hypoxia.** (**A**-**C**) Hypoxia inhibits the
463 effects of HIF-1α stabilization on glycolysis. Lung fibroblasts (LFs) were cultured in standard growth medium and
464 treated with molidustat (BAY, 10 μM) or vehicle (DMSO, 0.1%) in 21% or 0.5% oxygen conditions (n = 4). (A)
465 Growth rates were determined by linear fitting of log-transformed growth curves. (**B**-**C**) Extracellular fluxes of
466 glucose (note reversed *y*-axis) (B) and lactate (C). (**D**) Principal components analysis of intracellular metabolites
467 following 72 h of treatment described above suggests a dominant effect of hypoxia over PHD inhibition on the
468 metabolome (n = 4). (**E**) Volcano plot of the differential effects of hypoxia and molidustat (BAY) treatment on
469 intracellular metabolites. *Blue* circles indicate the fold change with hypoxia was greater than the fold change
470 with BAY treatment while *purple* circles indicate the opposite. (**F**) Representative metabolites highlighted in (E)
471 reveal different patterns of metabolic effects. (**G**) Metabolite set enrichment analysis of metabolites from (E).
472 KEGG pathways with p-values < 0.05 are shown. (**H**) Leading edge analysis of the most enriched KEGG
473 metabolite set from (G). Negative values indicate relative enrichment associated with BAY treatment compared
474 to hypoxia treatment (as in (E)). Abbreviations: PYR, pyruvate; SUC, succinate; PEP, phosphoenolpyruvate; CIT,
475 citrate; AKG, α-ketoglutarate; MAL, malate; ACO, aconitate; FUM, fumarate. (**I**-**K**) Intracellular NAD^+, NADH, and
476 their ratio were determined by enzymatic assay (n = 5). Black * indicate a significant effect of hypoxia, colored *
477 indicate a significant effect of treatment within a given oxygen tension as indicated by the color. Comparisons
478 for fluxes (A-C) and NAD(H) measurements (I-K) were performed using a mixed-effects linear model with
479 replicate as a random effect. Adjusted p-values for the indicated comparisons were determined using Tukey's
480 *post hoc* test.

481 Figure 6: **Transcriptomic analysis of molidustat treamtent in normoxia and hypoxia.** (**A**) Principal components
482 analysis of transcriptional changes following 72 h of treatment with 0.5% oxygen or molidustat (BAY), separately
483 or together (n = 4). (**B**) Volcano plot of the differential effects of hypoxia and molidustat (BAY) treatment on
484 intracellular metabolites. (**C**) Representative transcripts from (B). (**D**) Gene set enrichment analysis of transcripts
485 from (B). (**E**) Transcription factor enrichment analysis suggests mechanisms for differential regulation of gene
486 expression following hypoxia or BAY treatment.

487 Figure 7: **MYC regulates HIF-dependent glycolytic flux.** (**A**) Representative immunoblot of MYC protein
488 expression in lung fibroblsts following 72 h of treatment with 0.5% oxygen or molidustat (BAY, B). (**B**)
489 Quantification of immunoblots shown in (A). (**C**) Representative immunoblot of lung fibroblasts (LFs) treated
490 with siRNA targeting MYC (M) demonstrating adequate protein knockdown. (**D**) Growth rates of MYC-

491 knockdown cells cultured in hypoxia. (**E**) Lactate efflux rates of MYC-knockdown cells cultured in hypoxia. (**F**)
492 Representative immunoblot of LFs treated with MYC adenovirus. (**G**) Growth rates of MYC overexpressing cells
493 cultured with BAY. (**H**) Lactate efflux rates of MYC overexpressing cells cultured with BAY. Data are mean
494 Comparisons were performed using a mixed-effects linear model with replicate as a random effect. Adjusted p-
495 values for the indicated comparisons were determined using Tukey's *post hoc* test. Black * indicates a significant
496 effect of treatment, colored * indicate a significant effect of oxygen within a given treatment as indicated by the
497 color. Data are mean ± SEM of n = 4-5 biological replicates. Comparisons were made using linear mixed effects
498 models with treatment group as a fixed effect and biological replicate as a random effect. The multivariate *t*
499 distribution was used to determine significant differences as indicated by black * for difference within groups
500 defined by the x-axis and colored * for differences between groups defined by the x-axis as indicated by the
501 color with adjusted p-values < 0.05 considered significant.

502

Figures

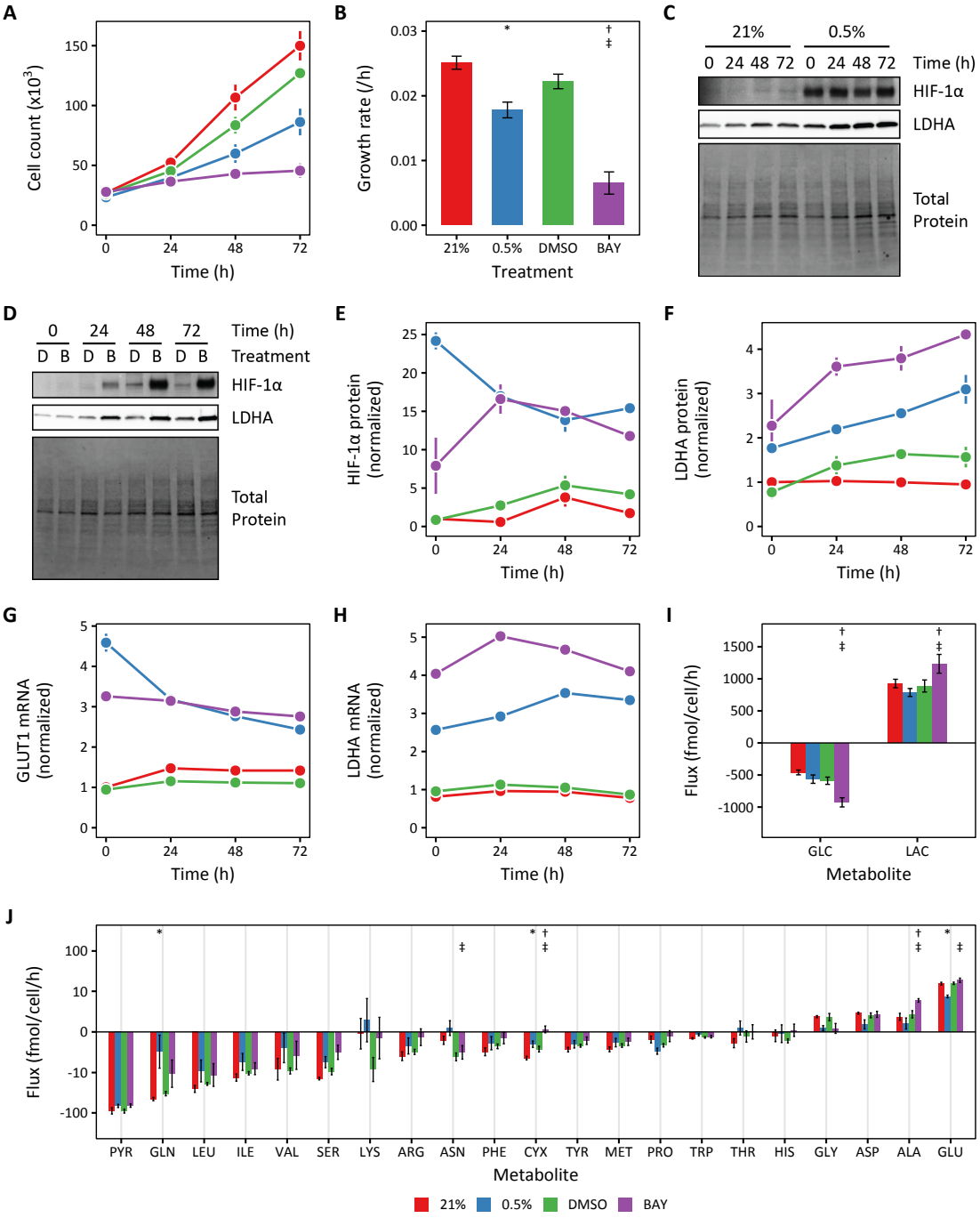

Figure 1: **Effects of prolyl hydroxylase inhibition on extracellular metabolite fluxes in lung fibroblasts.** Lung fibroblasts (LFs) were cultured with 21% oxygen (*red*), 0.5% oxygen (*blue*), DMSO (0.1% v/v, *green*), or molidustat (BAY, 10 µM, *purple*) beginning 24 h prior to time 0. (**A**) Growth curves of LFs in each experimental condition (n = 8). (**B**) Growth rates from (A) were determined by robust linear modeling of log-transformed growth curves. (**C**, **D**) Representative immunoblots of LF protein lysates cultured as in (A). (**E**, **F**) Relative change in HIF-1α (E) and LDHA (F) protein levels normalized to 21% oxygen or DMSO treatment time 0 (n = 4). (**G**, **H**) Relative changes in GLUT1 (G) and LDHA (H) mRNA levels normalized to 21% oxygen or DMSO treatment time 0 (n = 4). (**I**, **J**) Extracellular fluxes of the indicated metabolites (n = 8). Data are mean ± SEM. Comparisons were made using linear mixed effects models with treatment group as

512 a fixed effect and biological replicate as a random effect. Tukey's *post hoc* test was applied to determine differences between 21% and
513 0.5% oxygen (*), between DMSO and BAY treatment (†), or between 0.5% oxygen and BAY treatment (‡) with adjusted p-values < 0.05
514 considered significant.

515

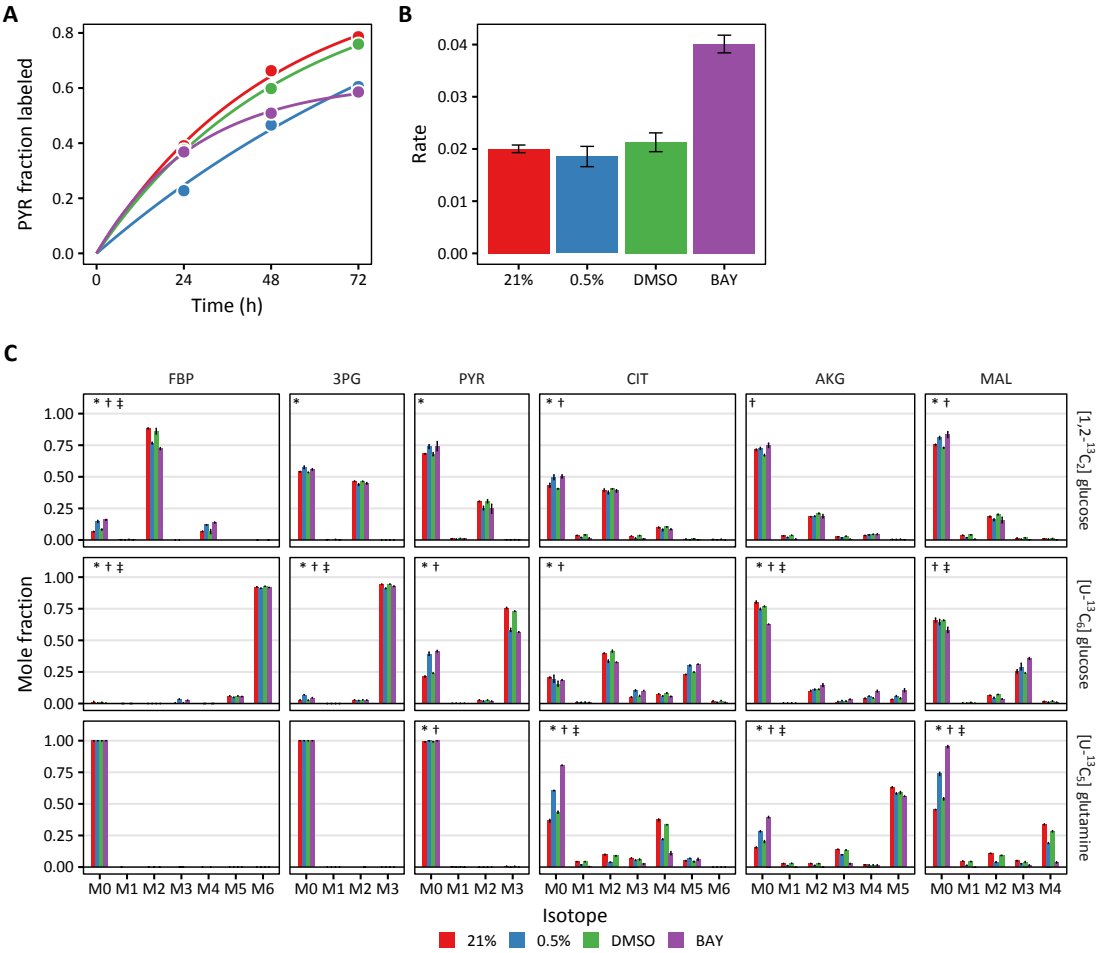

Figure 2: **Stable isotope tracing of lung fibroblasts.** (**A**) Fraction of pyruvate labeling following treatment of lung fibroblasts (LFs) with [U-$^{13}C_6$] glucose. (**B**) Rate values determined from asymptotic regression fit of the data from (A). (**C**) Isotopic labeling of key intracellular metabolites after 72 h of treatment with the indicated tracers. Experimentally determined mass isotope distributions were corrected for natural isotope abundance. Data are the mean ± SEM of 4 biological replicates. Significant differences in labeling patterns between 21% and 0.5% oxygen (*), DMSO and BAY treatment (†), and 0.5% oxygen and BAY treatment (‡) for each combination of metabolite and tracer are highlighted. FBP, fructose bisphosphate; 3PG, 3-phosphoglycerate; AKG, α-ketoglutarate.

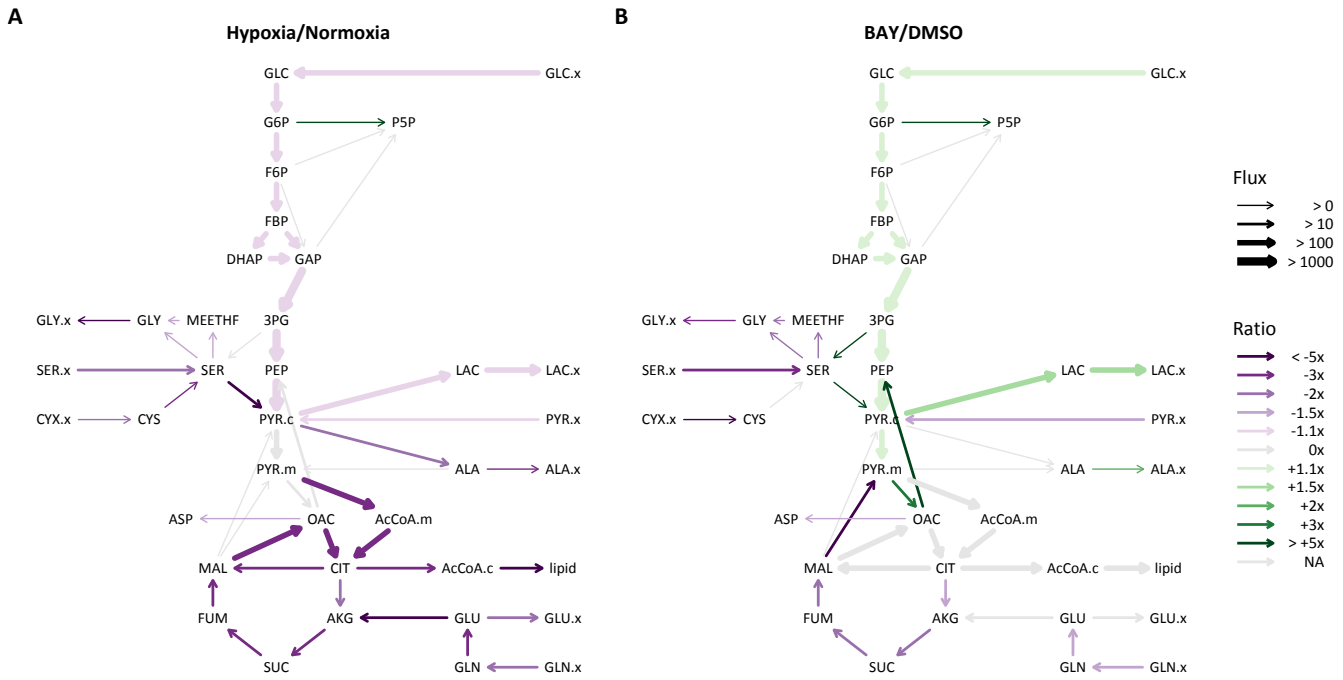

Figure 3: **Metabolic flux maps of lung fibroblasts.** (**A**) Ratio of metabolic fluxes in 0.5% oxygen compared to 21% oxygen. (**B**) Ratio of metabolic fluxes in cells treated with molidustat (BAY) compared to DMSO vehicle control. Fluxes with non-overlapping confidence intervals are highlighted with colored arrows to indicate significant changes. Arrow thickness corresponds to absolute flux in hypoxia- or BAY-treated cells.

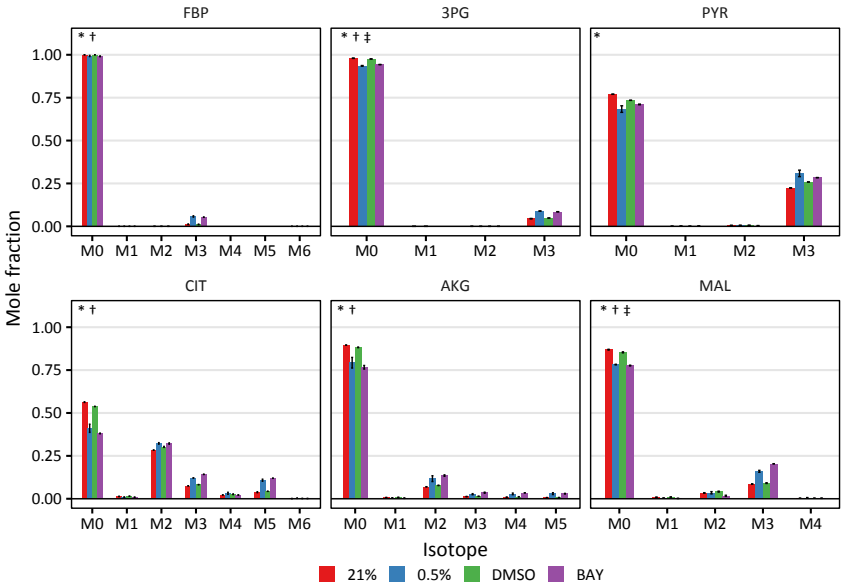

530

531 Figure 4: **PHD inhibition increases lactate uptake and oxidation.** Mass isotopomer distributions of key metabolites following labeling
532 with [U-$^{13}C_3$] lactate (2 mM) for 72 h indicates increased lactate uptake and oxidation in hypoxia or with molidustat (BAY) treatment. Data
533 are mean ± SEM of n = 4 biological replicates. Comparisons were made using linear mixed effects models with treatment group as a fixed
534 effect and biological replicate as a random effect. Tukey's *post hoc* test was applied to determine differences between 21% and 0.5%
535 oxygen (*), between DMSO and BAY treatment (†), or between 0.5% oxygen and BAY treatment (‡) with adjusted p-values < 0.05
536 considered significant.

537

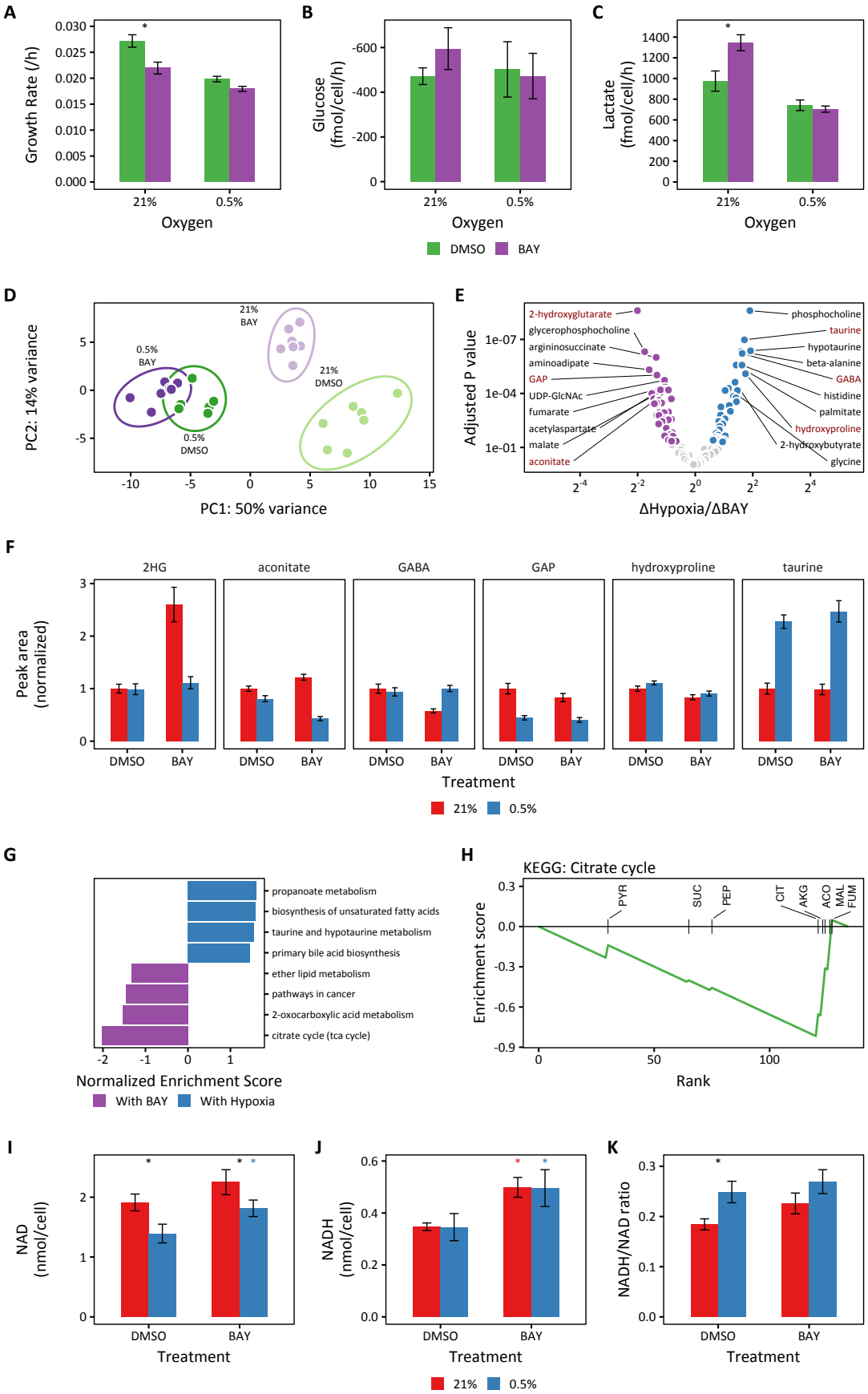
A
Growth Rate (/h)
0.030
0.025
0.020
0.015
0.010
0.005
0.000
21%
0.5%
Oxygen
B
Glucose (fmol/cell/h)
-600
-400
-200
0
21%
0.5%
Oxygen
C
Lactate (fmol/cell/h)
1400
1200
1000
800
600
400
200
0
21%
0.5%
Oxygen
DMSO
BAY
D
PC2: 14% variance
PC1: 50% variance
0.5% BAY
21% BAY
21% DMSO
0.5% DMSO
E
Adjusted P value
1e-07
1e-04
1e-01
ΔHypoxia/ΔBAY
2-hydroxyglutarate
glycerophosphocholine
argininosuccinate
aminoadipate
GAP
UDP-GlcNAc
fumarate
acetylaspartate
malate
aconitate
phosphocholine
taurine
hypotaurine
beta-alanine
GABA
histidine
palmitate
hydroxyproline
2-hydroxybutyrate
glycine
F
2HG
aconitate
GABA
GAP
hydroxyproline
taurine
Peak area (normalized)
DMSO
BAY
Treatment
21%
0.5%
G
propanoate metabolism
biosynthesis of unsaturated fatty acids
taurine and hypotaurine metabolism
primary bile acid biosynthesis
ether lipid metabolism
pathways in cancer
2-oxocarboxylic acid metabolism
citrate cycle (tca cycle)
Normalized Enrichment Score
With BAY
With Hypoxia
H
KEGG: Citrate cycle
PYR
SUC
PEP
CIT
AKG
ACO
MAL
FUM
Enrichment score
Rank
I
NAD (nmol/cell)
J
NADH (nmol/cell)
K
NADH/NAD ratio
DMSO
BAY
Treatment
21%
0.5%

539 Figure 5: **Metabolomic analysis of molidustat treatment in normoxia and hypoxia.** (**A**-**C**) Hypoxia inhibits the effects of HIF-1α
540 stabilization on glycolysis. Lung fibroblasts (LFs) were cultured in standard growth medium and treated with molidustat (BAY, 10 μM) or
541 vehicle (DMSO, 0.1%) in 21% or 0.5% oxygen conditions (n = 4). (A) Growth rates were determined by linear fitting of log-transformed
542 growth curves. (**B**-**C**) Extracellular fluxes of glucose (note reversed *y*-axis) (B) and lactate (C). (**D**) Principal components analysis of
543 intracellular metabolites following 72 h of treatment described above suggests a dominant effect of hypoxia over PHD inhibition on the
544 metabolome (n = 4). (**E**) Volcano plot of the differential effects of hypoxia and molidustat (BAY) treatment on intracellular metabolites.
545 *Blue* circles indicate the fold change with hypoxia was greater than the fold change with BAY treatment while *purple* circles indicate the
546 opposite. (**F**) Representative metabolites highlighted in (E) reveal different patterns of metabolic effects. (**G**) Metabolite set enrichment
547 analysis of metabolites from (E). KEGG pathways with p-values < 0.05 are shown. (**H**) Leading edge analysis of the most enriched KEGG
548 metabolite set from (G). Negative values indicate relative enrichment associated with BAY treatment compared to hypoxia treatment (as
549 in (E)). Abbreviations: PYR, pyruvate; SUC, succinate; PEP, phosphoenolpyruvate; CIT, citrate; AKG, α-ketoglutarate; MAL, malate; ACO,
550 aconitate; FUM, fumarate. (**I**-**K**) Intracellular NAD^+, NADH, and their ratio were determined by enzymatic assay (n = 5). Black * indicate a
551 significant effect of hypoxia, colored * indicate a significant effect of treatment within a given oxygen tension as indicated by the color.
552 Comparisons for fluxes (A-C) and NAD(H) measurements (I-K) were performed using a mixed-effects linear model with replicate as a
553 random effect. Adjusted p-values for the indicated comparisons were determined using Tukey's *post hoc* test.

554

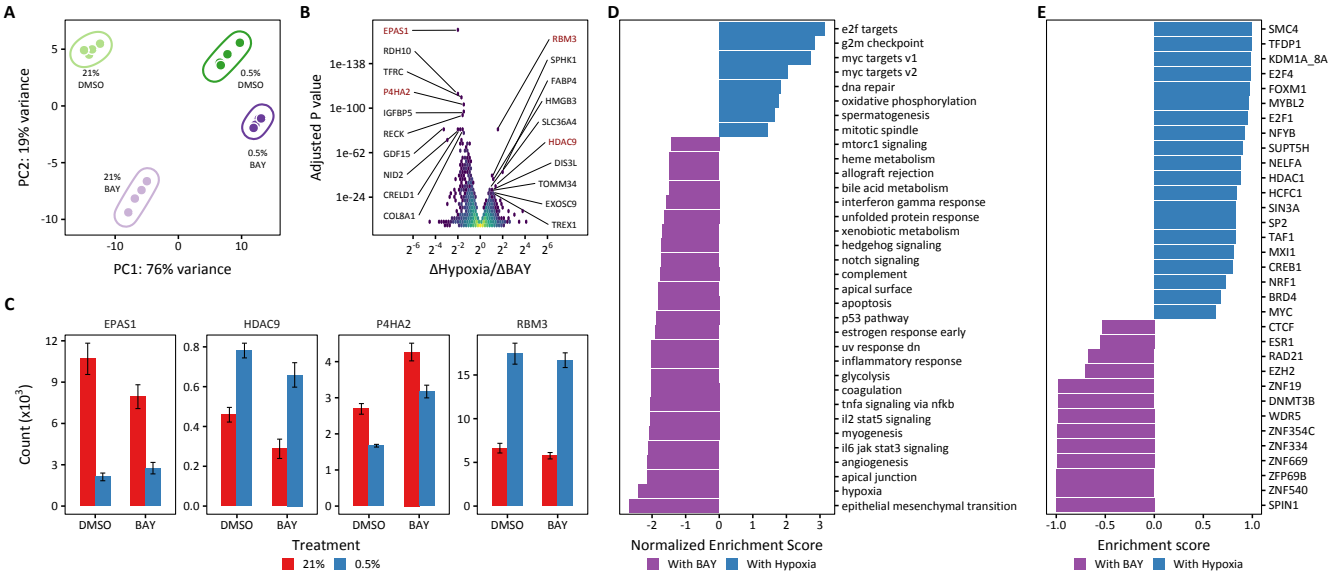

Figure 6: **Transcriptomic analysis of molidustat treamtent in normoxia and hypoxia.** (**A**) Principal components analysis of transcriptional changes following 72 h of treatment with 0.5% oxygen or molidustat (BAY), separately or together (n = 4). (**B**) Volcano plot of the differential effects of hypoxia and molidustat (BAY) treatment on intracellular metabolites. (**C**) Representative transcripts from (B). (**D**) Gene set enrichment analysis of transcripts from (B). (**E**) Transcription factor enrichment analysis suggests mechanisms for differential regulation of gene expression following hypoxia or BAY treatment.

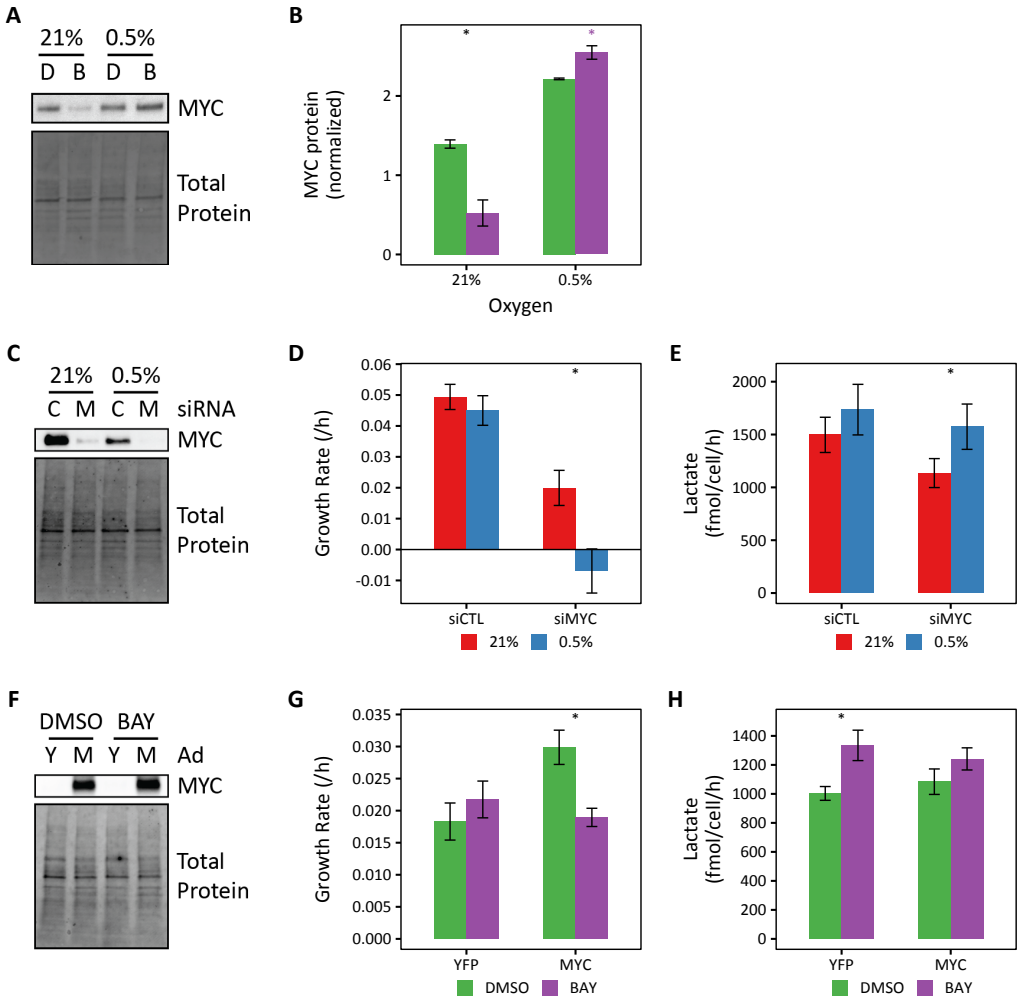

Figure 7: **MYC regulates HIF-dependent glycolytic flux.** (**A**) Representative immunoblot of MYC protein expression in lung fibroblsts following 72 h of treatment with 0.5% oxygen or molidustat (BAY, B). (**B**) Quantification of immunoblots shown in (A). (**C**) Representative immunoblot of lung fibroblasts (LFs) treated with siRNA targeting MYC (M) demonstrating adequate protein knockdown. (**D**) Growth rates of MYC-knockdown cells cultured in hypoxia. (**E**) Lactate efflux rates of MYC-knockdown cells cultured in hypoxia. (**F**) Representative immunoblot of LFs treated with MYC adenovirus. (**G**) Growth rates of MYC overexpressing cells cultured with BAY. (**H**) Lactate efflux rates of MYC overexpressing cells cultured with BAY. Data are mean Comparisons were performed using a mixed-effects linear model with replicate as a random effect. Adjusted p-values for the indicated comparisons were determined using Tukey's *post hoc* test. Black * indicates a significant effect of treatment, colored * indicate a significant effect of oxygen within a given treatment as indicated by the color. Data are mean ± SEM of n = 4-5 biological replicates. Comparisons were made using linear mixed effects models with treatment group as a fixed effect and biological replicate as a random effect. The multivariate *t* distribution was used to determine significant differences as indicated by black * for difference within groups defined by the x-axis and colored * for differences between groups defined by the x-axis as indicated by the color with adjusted p-values < 0.05 considered significant.

576 # STAR Methods

577 ## Resource Availability

578 ### Lead Contact

579 Further information and requests for resources and reagents should be directed to and will be fulfilled by the
580 lead contact, William Oldham (**woldham@bwh.harvard.edu**).

581 ### Materials Availability

582 This study did not generate new unique reagents.

583 ### Data and code availability

584 The original data and analysis code are available as a reproducible research compendium formatted as an R
585 package available at OldhamLab/Copeland.2021.hypoxia.flux
586 (**https://github.com/oldhamlab/Copeland.2021.hypoxia.flux**). RNA-seq data has been deposited in the NIH
587 Short Read Archive (PRJNA721596).

588 ## Experimental Model Details

589 ### Lung fibrolbasts

590 Primary normal human lung fibroblasts (LFs) were purchased from Lonza (CC-2512) and cultured in FGM-2
591 (Lonza CC-3132) in a standard tissue culture incubator in 5% CO_2 at 37 °C. Cells from two donors were used in
592 these studies: #33652 (56 y.o., male) and #29132 (19 y.o., female). Cell authentication was performed by the
593 vendor.

594 ### Pulmonary artery smooth muscle cells

595 Primary human pulmonary artery smooth muscle cells were purchased from Lonza (CC-2581) and cultured in
596 SmGM-2 (Lonza CC-3182) in a standard tissue culture incubator in 5% CO_2 at 37 °C. Cells from multiple donors
597 were used in these studies: #30020 (64 y.o., male), #27662 (35 y.o., male), #26698 (51 y.o., male), and #19828
598 (51 y.o., male). Cell authentication was performed by the vendor.

599 # Method Details

600 **Metabolic flux protocol**

601 For extracellular flux measurements, cells were seeded in either standard growth medium or MCDB131 medium
602 without glucose, glutamine, or phenol red (genDEPOT) supplemented with 2% dialyzed fetal bovine serum
603 (Mediatech) and naturally labeled glucose and glutamine ("light" labeling medium). For LFs, glucose was
604 supplemented at 8 mM and glutamine was supplemented at 1 mM. For PASMCs, glucose was supplemented at
605 5.55 mM and glutamine was supplemented at 10 mM. These concentrations match the concentrations of these
606 substrates determined in standard growth medium. Preliminary experiments were performed to identify the
607 optimal cell seeding density, exponential growth phase, and labeling duration consistent with metabolic and
608 isotopic steady state. On Day -1, 25,000 cells were seeded in a 35 mm dish in "light" labeling medium. Hypoxia-
609 treated cells were transferred to a tissue culture glovebox set to 0.5% oxygen and 5% CO_2 (Coy Lab Products).
610 Medium was supplemented with DMSO 0.1% or BAY (10 µM) for DMSO and BAY treatment conditions. On Day
611 0, cells were washed with PBS and the medium was changed to either "light" medium for flux measurements or
612 "heavy" medium for tracer experiments. For LFs, samples were collected on Day 0 and every 24 h for 72 h. For
613 PASMCs, samples were collected on Day 0 and every 12 h for 48 h. Medium and cell lysates were collected at
614 each time point for intra- and extracellular metabolite measurements and total DNA quantification. Dishes
615 without cells were weighed daily to correct for evaporative medium losses and to empirically determine
616 degradation and accumulation rates of metabolites. Medium samples and cell lysates for DNA measurement
617 were stored at -80 °C until analysis. Each individual experiment included triplicate wells for each treatment and
618 time point, and each experiment was repeated 4-8 times.

619 **Cell count**

620 Direct cell counts of trypsizined cell suspensions in PBS were obtained following staining with propidium iodide
621 and acridine orange using a LUNA-FL fluorescence cell counter (Logos Biosystems). Indirect cell counts for flux
622 measurements were interpolated from total DNA quantified using the Quant-iT PicoGreen dsDNA Assay Kit
623 (Thermo). Cells were washed once with two volumes of PBS, lysed with Tris-EDTA buffer containing 2% Triton X-
624 100, and collected by scraping. Total DNA in 10 µL of lysate was determined by adding 100 µL of 1X PicoGreen
625 dye in Tris-EDTA buffer and interpolating the fluorescence intensity with a standard curve generated using the λ
626 DNA standard. Cell counts were interpolated from a standard curve of DNA obtained from known cell numbers
627 seeded in basal medium (**Figure S1A**). No difference in total cellular DNA was identified between normoxia and
628 hypoxia cultures (**Figure S1B**).

629 **Immunoblots**

630 Cells were washed with one volume of PBS and collected by scraping in PBS. Cell suspensions were centrifuged
631 at 5,000 ×*g* for 5 min at 4 °C. Pellets were lysed in buffer containing Tris 10 mM, pH 7.4, NaCl 150 mM, EDTA 1
632 mM, EGTA 1 mM, Triton X-100 1% v/v, NP-40 0.5% v/v, and Halt Protease Inhibitor Cocktail (Thermo). Protein
633 concentrations were determined by BCA Protein Assay (Thermo). Lysates were normalized for protein
634 concentration and subjected to SDS-PAGE separation on stain-free tris-glycine gels (Bio-Rad), cross-linked and
635 imaged with the Chemidoc system (Bio-Rad), transferred to PVDF membranes with the Trans-Blot Turbo transfer
636 system (Bio-Rad), imaged, blocked in 5% blocking buffer (Bio-Rad), blotted in primary and secondary antibodies,
637 and developed using WesternBright ECL (Advansta). Band signal intensity was normalized to total protein per
638 lane as determined from the stain-free gel or membrane images.

639 **RT-qPCR**

640 Total RNA was isolated from cells with the RNeasy Mini Kit (Qiagen). cDNA was synthesized from 0.25-1.00 ng
641 RNA with the High Capacity cDNA Reverse Transcription Kit (Applied Biosystems). RT-qPCR analysis was
642 performed with an Applied Biosystems 7500 Fast Real Time PCR System with TaqMan Universal PCR Master Mix
643 and pre-designed TaqMan gene expression assays (Life Technologies). Relative expression levels were calculated
644 using the comparative cycle threshold method referenced to *ACTB*.

645 **Glucose assay**

646 Medium samples were diluted 10-fold in PBS. Glucose concentration was determined using the Glucose
647 Colorimetric Assay Kit (Cayman) according to the manufacturer's protocol. Standards were prepared in PBS.

648 **Lactate assay**

649 Medium samples were diluted 10-fold in PBS. Glucose concentration was determined using the L-Lactate Assay
650 Kit (Cayman). Medium samples did not require deproteinization, otherwise the samples were analyzed
651 according to the manufacturer's protocol. Standards were prepared in PBS.

652 **Pyruvate assay**

653 Pyruvate was measured using either an enzymatic assay (most samples) or an HPLC-based assay (medium from
654 0.2% oxygen experiments). For the enzymatic assay, medium samples were diluted 20-fold in PBS. Pyruvate
655 concentration was determined using the Pyruvate Assay Kit (Cayman). Medium samples did not require
656 deproteinization, otherwise the samples were analyzed according to the manufacturer's protocol. Standards

657 were prepared in PBS. For the HPLC assay, 2-oxovaleric acid was added to medium samples as an internal
658 standard. Samples were subsequently deproteinized with 2 volumes of ice-cold acetone. Supernatants were
659 evaporated to < 50% of the starting volume at 43 °C in a SpeedVac concentrator (Thermo Savant) and
660 reconstituted to the starting volume with HPLC-grade water prior to derivatization. Samples were derivatized
661 1:1 by volume with *o*-phenylenediamine (25 mM in 2 M HCl) for 30 min at 80 °C. Derivatized pyruvate was
662 separated with a Poroshell HPH C-18 column (2.1 × 100 mm, 2.7 µm) on an Infinity II high-performance liquid
663 chromatography system with fluorescence detection of OPD-derivatized α-keto acids as described previously
664 (**Guarino et al., 2019**).

665 **Amino acid assay**

666 Medium amino acid concentrations were determined following the addition of norvaline and sarcosine internal
667 standards and deproteinization with 2 volumes of ice-cold acetone. Supernatants were evaporated to < 50% of
668 the starting volume at 43 °C in a SpeedVac concentrator (Thermo Savant) and reconstituted to the starting
669 volume with HPLC-grade water prior to analysis. Amino acids in deproteinized medium were derivatized with *o*-
670 phthalaldehyde (OPA) and 9-fluorenylmethylchloroformate (FMOC) immediately prior to separation with a
671 Poroshell HPH-C18 column (4.6 × 100 mm, 2.7 µm) on an Infinity II high-performance liquid chromatography
672 system with ultraviolet and fluorescence detection of OPA- and FMOC-derivatized amino acids, respectively,
673 according to the manufacturer's protocol (Agilent) (**Long, 2017**).

674 **MYC knockdown**

675 Approximately 1.25 M lung fibroblasts were reverse transfected in 6-cm dishes with 40 pmol siMYC or non-
676 targeting siCTL pools (Dharmacon) in 20 uL RNAiMAX (Thermo). After 24 h, cells were collected by trypsinization
677 and re-seeded as described in *Metabolic flux protocol* above for growth rate and lactate efflux measurements.

678 **MYC overexpression**

679 Lung fibroblasts were seeded at 25,000 cells per 35 mm dish on Day -2. On Day -1, cells were transduced with
680 adenovirus for MYC (Vector Biolabs) or YFP overexpression (**Oldham et al., 2015**). After 24 h, the medium was
681 changed and samples were collected as described in *Metabolic flux protocol* above.

682 **Flux calculations**

683 The growth rate (μ) and flux (v) for each measured metabolite were defined as follows (**Murphy and Young,**
684 **2013**):

685
$$\frac{dX}{dt} = \mu X \qquad (1)$$
$$\frac{dM}{dt} = -kM + vX \qquad (2)$$

686 where *X* is the cell density, *k* is the first-order degradation or accumulation rate, and *M* is the mass of the
687 metabolite. These equations are solved as follows:

688
$$X = X_0 e^{\mu t} \qquad (3)$$
$$Me^{kt} = \frac{vX_0}{\mu + k}\left(e^{(\mu+k)t} - 1\right) + M_0 \qquad (4)$$

689 Growth rate (μ) and cell count at time 0 (X_0) were determined by robust linear modeling of the logarithm of cell
690 count as a function of time (t). Metabolite mass was calculated from the measured metabolite concentrations
691 and predicted well volume accounting for evaporative losses (**Figure S1C**). First-order degradation and
692 accumulation rates were obtained from robust linear modeling of metabolite mass *v*. time in unconditioned
693 culture medium. Rates that significantly differed from 0 using Student's *t*-test were incorporated into the flux
694 calculations. Final fluxes were obtained by robust linear modeling of Me^{kt} *versus* $\left(e^{(\mu+k)t} - 1\right)$ to determine
695 the slope from which v was calculated using equation (4).

696 **Metabolomics**

697 *Metabolite extraction*

698 Intracellular metabolites were obtained after washing cells with 2 volumes of ice-cold PBS and floating on liquid
699 nitrogen. Plates were stored at -80 °C until extraction. Metabolites were extracted with 1 mL 80% MeOH pre-
700 cooled to -80 °C containing 10 nmol [D_8]-valine as an internal standard (Cambridge Isotope Labs). Insoluble
701 material was removed by centrifugation at 21,000 ×*g* for 15 min at 4 °C. The supernatant was evaporated to
702 dryness at 42 °C using a SpeedVac concentrator (Thermo Savant). Samples were resuspended in 35 µL LC-MS-
703 grade water prior to analysis.

704 *Acquisition parameters*

705 LC-MS analysis was performed on a Vanquish ultra-high-performance liquid chromatography system coupled to
706 a Q Exactive orbitrap mass spectrometer by a HESI-II electrospray ionization probe (Thermo). External mass
707 calibration was performed weekly. Metabolite samples (2.5 µL) were separated using a ZIC-pHILIC stationary
708 phase (2.1 × 150 mm, 5 µm) (Merck). The autosampler temperature was 4 °C and the column compartment was
709 maintained at 25 °C. Mobile phase A was 20 mM ammonium carbonate and 0.1% ammonium hydroxide. Mobile

710 phase B was acetonitrile. The flow rate was 0.1 mL/min. Solvent was introduced to the mass spectrometer *via*
711 electrospray ionization with the following source parameters: sheath gas 40, auxiliary gas 15, sweep gas 1, spray
712 voltage +3.0 kV for positive mode and -3.1 kV for negative mode, capillary temperature 275 °C, S-lens RF level
713 40, and probe temperature 350 °C. Data were acquired and peaks integrated using TraceFinder 4.1 (Thermo).

714 *Stable isotope quantification*

715 All metabolites except fructose 2,6-bisphosphate (FBP) and 3-phosphoglycerate (3PG) were measured using the
716 following mobile phase gradient: 0 min, 80% B; 5 min, 80% B; 30 min, 20% B; 31 min, 80% B; 42 min, 80% B. The
717 mass spectrometer was operated in selected ion monitoring mode with an m/*z* window width of 9.0 centered
718 1.003355-times half the number of carbon atoms in the target metabolite. The resolution was set at 70,000 and
719 AGC target was 1×10^5 ions. Peak areas were corrected for quadrupole bias as previously described (**Kim et al.,**
720 **2015**). Mass isotope distributions for FBP and 3PG were calculated from full scan chromatograms as described
721 below. Raw mass isotopomer distributions were corrected for natural isotope abundance using a custom R
722 package (mzrtools, **https://github.com/oldhamlab/mzrtools**) employing the method of Fernandez, *et al.*
723 (**Fernandez et al., 1996**).

724 *Metabolomic profiling*

725 For metabolomic profiling and quantification of isotopic enrichment for FBP and 3PG, the following mobile
726 phase gradient was used: 0 min, 80% B; 20 min, 20% B; 20.5 min, 80% B; 28 min, 80% B; 42 min, 80% B. The
727 mass spectrometer was operated in polarity switching full scan mode from 70-1000 m/*z*. Resolution was set to
728 70,000 and the AGC target was $1x10^6$ ions. Peak identifications were based on an in-house library of authentic
729 metabolite standards previously analyzed utilizing this method. For metabolomics studies, pooled quality control
730 (QC) samples were injected at the beginning, end, and between every four samples of the run. Raw peak areas
731 for each metabolite were corrected for instrument drift using a cubic spline model of QC peak areas. Low quality
732 features were removed on the basis of a relative standard deviation greater than 0.2 in the QC samples and a
733 dispersion ratio greater than 0.4 (**Broadhurst et al., 2018**). Missing values were imputed using random forest.
734 Samples peak areas were normalized using probabilistic quotient normalization (**Dieterle et al., 2006**).
735 Differentially regulated metabolites were identified using limma (**Ritchie et al., 2015**). Metabolite set
736 enrichment analysis was performed using the fgsea package with metabolite pathways downloaded using
737 multiGSEA (**Korotkevich et al., 2019**; **Sebastian and Hackermüller, 2020**).

738 **Biomass determination**

739 The dry weight of LFs was determined to be 493 pg/cell. The dry weight of PASMCs was determined to be 396
740 pg/cell. These values were estimated by washing 3×10^6 cells twice in PBS and thrice in ice-cold acetone prior to
741 drying overnight in a SpeedVac. The composition of the dry cell mass was estimated from the literature (**Quek et**
742 **al., 2010**; **Sheikh et al., 2005**), and stoichiometric coefficients were determined as described (**Murphy et al.,**
743 **2013**; **Zamorano et al., 2010**).

744 **Metabolic flux analysis**

745 Metabolic flux analysis was performed using the elementary metabolite unit-based software package INCA
746 (**Young, 2014**). Inputs to the model include the chemical reactions and atom transitions of central carbon
747 metabolism, extracellular fluxes, the identity and composition of ^{13}C-labeled tracers, and the MIDs of labeled
748 intracellular metabolites. The metabolic network was adapted from previously published networks (**Murphy et**
749 **al., 2013**; **Vacanti et al., 2014**) and comprises 48 reactions representing glycolysis, the pentose phosphate
750 pathway, the tricarboxylic acid cycle, anaplerotic pathways, serine metabolism, and biomass synthesis. The
751 network includes seven extracellular substrates (aspartate, cystine, glucose, glutamine, glycine, pyruvate, serine)
752 and five metabolic products (alanine, biomass, glutamate, lactate, lipid). Models were fit using three ^{13}C-labeled
753 tracers, [1,2-$^{13}C_2$] glucose, [U-$^{13}C_6$] glucose, and [U-$^{13}C_5$] glutamine. The MIDs of twelve metabolites (2-
754 oxoglutarate, 3-phosphoglycerate, alanine, aspartate, citrate, fructose bisphosphate, glutamate, glutamine,
755 lactate, malate, pyruvate, serine) were used to constrain intracellular fluxes. The following assumptions were
756 made:

757 1. Metabolism was at steady state.
758 2. Labeled CO_2 produced during decarboxylation reactions left the system and did not re-incorporate
759 during carboxylation reactions.
760 3. Protein turnover occurred at a negligible rate compared to glucose and glutamine consumption.
761 4. Acetyl-CoA, aspartate, fumarate, malate, oxaloacetate, and pyruvate existed in cytosolic and
762 mitochondrial pools. Aspartate and malate were allowed to exchange freely between the
763 compartments.
764 5. The per cell biomass requirements of proliferating lung fibroblasts were similar to published estimated
765 in other cells (**Quek et al., 2010**; **Sheikh et al., 2005**).

766 6. Dilution of alanine, aspartate, glutamate, glutamine, lactate, and pyruvate was allowed to occur through
767 reversible exchange with unlabeled substrates in the medium as these metabolites were present in
768 unconditioned medium or serum.
769 7. Succinate and fumarate are symmetric molecules that have interchangeable orientations when
770 metabolized by TCA cycle enzymes.

771 Flux estimation was repeated a minimum of 50 times from random initial values. Results were subjected to a χ^2
772 statistical test to assess goodness-of-fit. Accurate 95% confidence intervals were computed for estimated
773 parameters by evaluating the sensitivity of the sum-of-square residuals to parameter variations (**Antoniewicz et**
774 **al., 2006**; **Murphy et al., 2013**).

775 **NAD(H) assay**

776 Cellular NAD^+ and NADH were measured using an enzymatic fluorimetric cycling assay based on the reduction of
777 NAD^+ to NADH by alcohol dehydrogenase (ADH) and subsequent electron transfer to generate the fluorescent
778 molecule resorufin (**Oldham et al., 2015**). Briefly, cells were washed twice with one volume PBS. Pyridine
779 nucleotides were extracted on ice with buffer containing 50% by volume PBS and 50% lysis buffer (100 mM
780 sodium carbonate, 20 mM sodium bicarbonate, 10 mM nicotinamide, 0.05% by volume Triton-X-100, 1% by
781 mass dodecyltrimethylammonium bromide) and collected by scraping. Extracts were divided equally and 0.5
782 volume of 0.4 N HCl was added to one sample. Both extracts were heated at 65 °C for 15 min to degrade
783 selectively either the oxidized (buffer) or reduced (HCl) nucleotides. The reaction was cooled on ice and
784 quenched by adding 0.5 M Tris-OH to the acid-treated samples or 0.2 N HCl plus 0.25 M Tris-OH to the buffer
785 samples. Samples were then diluted in reaction buffer (50 mM EDTA and 10 mM Tris, pH 7.06). Cell debris was
786 pelleted by centrifugation, and 50 µL was incubated for 2 h with 100 µL reaction buffer containing 0.6 M EtOH,
787 0.5 mM phenazine methosulfate, 0.05 mM resazurin, and 0.1 mg/mL ADH. Fluorescence intensities were
788 measured with a Spectramax Gemini XPS (Moelcular Devices) with excitation 540 nm, emission 588 nm, and 550
789 nm excitation cut-off filter. Sample intensities were compared to a standard curve generated from known
790 concentrations of NADH. The ratio of fluorescence in buffer-extracted to acid-extracted samples corresponds to
791 the $NADH/NAD^+$ ratio. Absolute NADH and NAD^+ were normalized to cell count from cells estimated from total
792 DNA quantification as described above.

793 **RNA-seq**

794 RNA was collected from LFs treated for three days ± hypoxia ± BAY as described above. Four biological replicates
795 were analyzed. Library construction and sequencing was performed by BGI Genomics using 100 bp paired end

796 analysis and a read depth of 50M reads per sample. Sequences were deposited in the NIH SRA (PRJNA721596).
797 Sequences were mapped to the human GRCh38 primary assembly and counts summarized using Rsubread (**Liao**
798 **et al., 2019**). This data is available from the Oldham Lab GitHub repository
799 (**https://github.com/oldhamlab/rnaseq.lf.hypoxia.molidustat**). Differentially expressed transcripts were
800 identified using DESeq2 (**Love et al., 2014**). Gene set enrichment and transcription factor enrichment was
801 performed using the fgsea and TFEA.ChIP R packages, respectively (**Korotkevich et al., 2019**; **Puente-Santamaria**
802 **et al., 2019**).

803 Quantification and Statistical Analysis

804 The raw data and annotated analysis code necessary to reproduce this manuscript are contained in an R package
805 research compendium available from the Oldham Lab GitHub repository
806 (**https://github.com/oldhamlab/Copeland.2021.hypoxia.flux**). Data analysis, statistical comparisons, and
807 visualization were performed in R (**R Core Team, 2020**) using the packages referenced in the data supplement.
808 Experiments included technical and biological replicates as noted above. The number of biological replicates (n)
809 is indicated in the figure legends. Summary data show the mean ± SEM. Outliers were identified using twice the
810 median absolute deviation as a cutoff threshold. Two group comparisons (*e.g.*, 21% *v.* 0.5% oxygen) were
811 performed using Student's *t*-test on log-transformed values with pairing among biological replicates. Multifactor
812 comparisons (*e.g.*, BAY and oxygen) were performed using linear mixed-effects models with Tukey's *post hoc*
813 testing. Metabolomics and RNA-seq data were analyzed as described above. Probability values less than 0.05
814 were considered significant.

815

816 # Key Resources Table

817

REAGENT or RESOURCE	SOURCE	IDENTIFIER
Antibodies		
HIF-1α	BD Biosciences	610958
c-MYC	Cell Signaling Technologies	D84C12
LDHA	Cell Signaling Technologies	2012
HRP-α-Rabbit IgG	Cell Signaling Technologies	7074
HRP-α-Mouse IgG	Cell Signaling Technologies	7076
Bacterial and virus strains		
[1,2-$^{13}C_2$] glucose	Vector Biolabs	1285
[U-$^{13}C_6$] glucose	Oldham et al., 2015	
[U-$^{13}C_5$] glutamine		
[U-$^{13}C_3$] lactate	Cambridge Isotope Labs	CLM-504-PK
[U-^13^C~6~] glucose	Cambridge Isotope Labs	CLM-1396-PK
[U-^13^C~5~] glutamine	Cambridge Isotope Labs	CLM-1822-H-PK
[U-^13^C~3~] lactate	Sigma	485926
Molidustat (BAY-85-3934)	Cayman	15297
Critical commercial assays		
Glucose colorimetric assay kit	Cayman	10009582
L-Lactate assay kit	Cayman	700510
Pyruvate assay kit	Cayman	700470
Depositied data		
Raw and analyzed data	This paper	https://github.com/oldhamlab/Copeland.2021.hypoxia.flux
RNA-seq reads	This paper	SRA: PRJNA721596
Summarized RNA-seq data	This paper	https://github.com/oldhamlab/rnaseq.lf.hypoxia.molidustat
Experimental models: Cell lines		

REAGENT or RESOURCE	SOURCE	IDENTIFIER
Normal human lung fibroblasts	Lonza	CC-2512
Pulmonary artery smooth muscle cells	Lonza	CC-2581
Oligonucleotides		
ACTB (Hs03023943_g1)	Life Technologies	4351370
GLUT1 (Hs00892681_m1)	Life Technologies	4351370
LDHA (Hs00855332_g1)	Life Technologies	4351370
MYC ON-TARGETplus siRNA	Dharmacon	L-003282-02-0005
ON-TARGETplus non-targeting control pool	Dharmacon	D-001810-10-05

818

819 # Supplemental Items Titles

820 Table S1: **Lung fibroblast fluxes in 21% and 0.5% oxygen.**

821 Table S2: **Lung fibroblast fluxes following DMSO and BAY treatment.**

822 Table S3: **PASMC fluxes in 21% and 0.5% oxygen.**

823 Figure S1: **Supporting data for extracellular flux calculations.**

824 Figure S2: **Extracellular flux measurements in 0.2% oxygen.**

825 Figure S3: **Extracellular flux measurements in pulmonary artery smooth muscle cells in 0.5% oxygen.**

826 Figure S4: **Mass isotopomer distributions after 72 h of labeling in lung fibroblasts.**

827 Figure S5: **Mass isotopomer distributions after 72 h of labeling in pulmonary artery smooth muscle cells.**

828 Figure S6: **Isotope incorporation in key metabolites over the experimental time course.**

829 Figure S7: **Isotopically non-stationary metabolic flux analysis.**

830 Figure S8: **Metabolomic profiling of hypoxia and BAY treated lung fibroblasts.**

831 Figure S9: **Transcriptomic profiling of hypoxia and BAY treated lung fibroblasts.**

832

833 # References

834 Antoniewicz, M.R., Kelleher, J.K., and Stephanopoulos, G. (2006). Determination of confidence intervals of
835 metabolic fluxes estimated from stable isotope measurements. Metab Eng *8*, 324–337.

836 Batie, M., Frost, J., Frost, M., Wilson, J.W., Schofield, P., and Rocha, S. (2019). Hypoxia induces rapid changes to
837 histone methylation and reprograms chromatin. Science *363*, 1222–1226.

838 Broadhurst, D., Goodacre, R., Reinke, S.N., Kuligowski, J., Wilson, I.D., Lewis, M.R., and Dunn, W.B. (2018).
839 Guidelines and considerations for the use of system suitability and quality control samples in mass spectrometry
840 assays applied in untargeted clinical metabolomic studies. Metabolomics *14*, 72.

841 Chance, B., and Williams, G.R. (1955). Respiratory enzymes in oxidative phosphorylation. III. The steady state. J
842 Biol Chem *217*, 409–427.

843 Chandel, N.S., Maltepe, E., Goldwasser, E., Mathieu, C.E., Simon, M.C., and Schumacker, P.T. (1998).
844 Mitochondrial reactive oxygen species trigger hypoxia-induced transcription. Proc Natl Acad Sci U S A *95*, 11715–
845 11720.

846 Chen, C., Cai, S., Wang, G., Cao, X., Yang, X., Luo, X., Feng, Y., and Hu, J. (2013). C-Myc enhances colon cancer
847 cell-mediated angiogenesis through the regulation of HIF-1α. Biochem Biophys Res Commun *430*, 505–511.

848 Contreras-Baeza, Y., Sandoval, P.Y., Alarcon, R., Galaz, A., Cortes-Molina, F., Alegria, K., Baeza-Lehnert, F., Arce-
849 Molina, R., Guequen, A., Flores, C.A., et al. (2019). Monocarboxylate transporter 4 (MCT4) is a high affinity
850 transporter capable of exporting lactate in high-lactate microenvironments. J Biol Chem *294*, 20135–20147.

851 Dang, C.V. (2012). MYC on the path to cancer. Cell *149*, 22–35.

852 Dang, C.V., O'Donnell, K.A., Zeller, K.I., Nguyen, T., Osthus, R.C., and Li, F. (2006). The c-Myc target gene
853 network. Semin Cancer Biol *16*, 253–264.

854 Dieterle, F., Ross, A., Schlotterbeck, G., and Senn, H. (2006). Probabilistic quotient normalization as robust
855 method to account for dilution of complex biological mixtures. Application in 1H NMR metabonomics. Anal
856 Chem *78*, 4281–4290.

857 Doe, M.R., Ascano, J.M., Kaur, M., and Cole, M.D. (2012). Myc posttranscriptionally induces HIF1 protein and
858 target gene expression in normal and cancer cells. Cancer Res *72*, 949–957.

859 Fan, J., Kamphorst, J.J., Mathew, R., Chung, M.K., White, E., Shlomi, T., and Rabinowitz, J.D. (2013). Glutamine-
860 driven oxidative phosphorylation is a major ATP source in transformed mammalian cells in both normoxia and
861 hypoxia. Mol Syst Biol *9*, 712.

862 Faubert, B., Boily, G., Izreig, S., Griss, T., Samborska, B., Dong, Z., Dupuy, F., Chambers, C., Fuerth, B.J., Viollet, B.,
863 et al. (2013). AMPK is a negative regulator of the warburg effect and suppresses tumor growth in vivo. Cell
864 Metab *17*, 113–124.

865 Favaro, E., Bensaad, K., Chong, M.G., Tennant, D.A., Ferguson, D.J., Snell, C., Steers, G., Turley, H., Li, J.L.,
866 Gunther, U.L., et al. (2012). Glucose utilization via glycogen phosphorylase sustains proliferation and prevents
867 premature senescence in cancer cells. Cell Metab *16*, 751–764.

868 Fernandez, C.A., Des Rosiers, C., Previs, S.F., David, F., and Brunengraber, H. (1996). Correction of 13C mass
869 isotopomer distributions for natural stable isotope abundance. J Mass Spectrom *31*, 255–262.

870 Fessel, J.P., Hamid, R., Wittmann, B.M., Robinson, L.J., Blackwell, T., Tada, Y., Tanabe, N., Tatsumi, K., Hemnes,
871 A.R., and West, J.D. (2012). Metabolomic analysis of bone morphogenetic protein receptor type 2 mutations in
872 human pulmonary endothelium reveals widespread metabolic reprogramming. Pulm Circ *2*, 201–213.

873 Flamme, I., Oehme, F., Ellinghaus, P., Jeske, M., Keldenich, J., and Thuss, U. (2014). Mimicking hypoxia to treat
874 anemia: HIF-stabilizer BAY 85-3934 (molidustat) stimulates erythropoietin production without hypertensive
875 effects. PLoS One *9*, e111838.

876 Gameiro, P.A., Yang, J., Metelo, A.M., Perez-Carro, R., Baker, R., Wang, Z., Arreola, A., Rathmell, W.K., Olumi, A.,
877 Lopez-Larrubia, P., et al. (2013). In vivo HIF-mediated reductive carboxylation is regulated by citrate levels and
878 sensitizes VHL-deficient cells to glutamine deprivation. Cell Metab *17*, 372–385.

879 Garcia-Bermudez, J., Baudrier, L., La, K., Zhu, X.G., Fidelin, J., Sviderskiy, V.O., Papagiannakopoulos, T., Molina,
880 H., Snuderl, M., Lewis, C.A., et al. (2018). Aspartate is a limiting metabolite for cancer cell proliferation under
881 hypoxia and in tumours. Nat Cell Biol *20*, 775–781.

882 Gardner, L.B., Li, Q., Park, M.S., Flanagan, W.M., Semenza, G.L., and Dang, C.V. (2001). Hypoxia inhibits G1/s
883 transition through regulation of p27 expression. J Biol Chem *276*, 7919–7926.

884 Garofalo, O., Cox, D.W., and Bachelard, H.S. (1988). Brain levels of NADH and NAD+ under hypoxic and
885 hypoglycaemic conditions in vitro. J Neurochem *51*, 172–176.

886 Gordan, J.D., Bertout, J.A., Hu, C.J., Diehl, J.A., and Simon, M.C. (2007). HIF-2alpha promotes hypoxic cell
887 proliferation by enhancing c-myc transcriptional activity. Cancer Cell *11*, 335–347.

888 Grassian, A.R., Parker, S.J., Davidson, S.M., Divakaruni, A.S., Green, C.R., Zhang, X., Slocum, K.L., Pu, M., Lin, F.,
889 Vickers, C., et al. (2014). IDH1 mutations alter citric acid cycle metabolism and increase dependence on oxidative
890 mitochondrial metabolism. Cancer Res *74*, 3317–3331.

891 Guarino, V.A., Oldham, W.M., Loscalzo, J., and Zhang, Y.Y. (2019). Reaction rate of pyruvate and hydrogen
892 peroxide: Assessing antioxidant capacity of pyruvate under biological conditions. Sci Rep *9*, 19568.

893 Guzy, R.D., Hoyos, B., Robin, E., Chen, H., Liu, L., Mansfield, K.D., Simon, M.C., Hammerling, U., and Schumacker,
894 P.T. (2005). Mitochondrial complex III is required for hypoxia-induced ROS production and cellular oxygen
895 sensing. Cell Metab *1*, 401–408.

896 Hubbi, M.E., and Semenza, G.L. (2015). Regulation of cell proliferation by hypoxia-inducible factors. Am J Physiol
897 Cell Physiol *309*, C775–82.

898 Hui, S., Ghergurovich, J.M., Morscher, R.J., Jang, C., Teng, X., Lu, W., Esparza, L.A., Reya, T., Le, Z., Yanxiang Guo,
899 J., et al. (2017b). Glucose feeds the TCA cycle via circulating lactate. Nature *551*, 115–118.

900 Hui, S., Ghergurovich, J.M., Morscher, R.J., Jang, C., Teng, X., Lu, W., Esparza, L.A., Reya, T., Le, Z., Yanxiang Guo,
901 J., et al. (2017a). Glucose feeds the TCA cycle via circulating lactate. Nature *551*, 115–118.

902 Hui, S., Cowan, A.J., Zeng, X., Yang, L., TeSlaa, T., Li, X., Bartman, C., Zhang, Z., Jang, C., Wang, L., et al. (2020).
903 Quantitative fluxomics of circulating metabolites. Cell Metab.

904 Hydbring, P., Castell, A., and Larsson, L.G. (2017). MYC modulation around the CDK2/p27/SKP2 axis. Genes
905 (Basel) *8*.

906 Islam, M.S., Leissing, T.M., Chowdhury, R., Hopkinson, R.J., and Schofield, C.J. (2018). 2-oxoglutarate-dependent
907 oxygenases. Annu Rev Biochem *87*, 585–620.

908 Jain, I.H., Calvo, S.E., Markhard, A.L., Skinner, O.S., To, T.L., Ast, T., and Mootha, V.K. (2020). Genetic screen for
909 cell fitness in high or low oxygen highlights mitochondrial and lipid metabolism. Cell *181*, 716–727 e11.

910 Jazmin, L.J., and Young, J.D. (2013). Isotopically nonstationary 13C metabolic flux analysis. Methods Mol Biol
911 *985*, 367–390.

912 Jiang, L., Shestov, A.A., Swain, P., Yang, C., Parker, S.J., Wang, Q.A., Terada, L.S., Adams, N.D., McCabe, M.T.,
913 Pietrak, B., et al. (2016). Reductive carboxylation supports redox homeostasis during anchorage-independent
914 growth. Nature *532*, 255–258.

915 Kaelin, Jr., W. G., and Ratcliffe, P.J. (2008). Oxygen sensing by metazoans: The central role of the HIF hydroxylase
916 pathway. Mol Cell *30*, 393–402.

917 Kim, D., Fiske, B.P., Birsoy, K., Freinkman, E., Kami, K., Possemato, R.L., Chudnovsky, Y., Pacold, M.E., Chen,
918 W.W., Cantor, J.R., et al. (2015). SHMT2 drives glioma cell survival in ischaemia but imposes a dependence on
919 glycine clearance. Nature *520*, 363–367.

920 Korotkevich, G., Sukhov, V., and Sergushichev, A. (2019). Fast gene set enrichment analysis. bioRxiv.

921 Koshiji, M., Kageyama, Y., Pete, E.A., Horikawa, I., Barrett, J.C., and Huang, L.E. (2004). HIF-1alpha induces cell
922 cycle arrest by functionally counteracting myc. EMBO J *23*, 1949–1956.

923 Lee, P., Chandel, N.S., and Simon, M.C. (2020). Cellular adaptation to hypoxia through hypoxia inducible factors
924 and beyond. Nat Rev Mol Cell Biol *21*, 268–283.

925 Lee, W.D., Mukha, D., Aizenshtein, E., and Shlomi, T. (2019). Spatial-fluxomics provides a subcellular-
926 compartmentalized view of reductive glutamine metabolism in cancer cells. Nat Commun *10*, 1351.

927 Li, F., Wang, Y., Zeller, K.I., Potter, J.J., Wonsey, D.R., O'Donnell, K.A., Kim, J.-W., Yustein, J.T., Lee, L.A., and Dang,
928 C.V. (2005). Myc stimulates nuclearly encoded mitochondrial genes and mitochondrial biogenesis. Mol Cell Biol
929 *25*, 6225–6234.

930 Li, Y., Sun, X.-X., Qian, D.Z., and Dai, M.-S. (2020). Molecular Crosstalk Between MYC and HIF in Cancer. Front Cell
931 Dev Biol *8*, 590576.

932 Liao, Y., Smyth, G.K., and Shi, W. (2019). The R package Rsubread is easier, faster, cheaper and better for
933 alignment and quantification of RNA sequencing reads. Nucleic Acids Research *47*, e47.

934 Liberzon, A., Birger, C., Thorvaldsdottir, H., Ghandi, M., Mesirov, J.P., and Tamayo, P. (2015). The molecular
935 signatures database (MSigDB) hallmark gene set collection. Cell Syst *1*, 417–425.

936 Long, W. (2017). Automated amino acid analysis using an agilent poroshell HPH-C18 column. Application Note,
937 Agilent Technologies, Inc. *Publication Number 5991-5571EN*, 1–10.

938 Love, M.I., Huber, W., and Anders, S. (2014). Moderated estimation of fold change and dispersion for RNA-seq
939 data with DESeq2. Genome Biology *15*, 550.

940 Madden, S.K., de Araujo, A.D., Gerhardt, M., Fairlie, D.P., and Mason, J.M. (2021). Taking the Myc out of cancer:
941 Toward therapeutic strategies to directly inhibit c-Myc. Molecular Cancer *20*, 3.

942 Masson, N., Keeley, T.P., Giuntoli, B., White, M.D., Puerta, M.L., Perata, P., Hopkinson, R.J., Flashman, E., Licausi,
943 F., and Ratcliffe, P.J. (2019). Conserved n-terminal cysteine dioxygenases transduce responses to hypoxia in
944 animals and plants. Science *365*, 65–69.

945 Melendez-Rodriguez, F., Urrutia, A.A., Lorendeau, D., Rinaldi, G., Roche, O., Bogurcu-Seidel, N., Ortega Muelas,
946 M., Mesa-Ciller, C., Turiel, G., Bouthelier, A., et al. (2019). HIF1alpha suppresses tumor cell proliferation through
947 inhibition of aspartate biosynthesis. Cell Rep *26*, 2257–2265 e4.

948 Metallo, C.M., Gameiro, P.A., Bell, E.L., Mattaini, K.R., Yang, J., Hiller, K., Jewell, C.M., Johnson, Z.R., Irvine, D.J.,
949 Guarente, L., et al. (2011). Reductive glutamine metabolism by IDH1 mediates lipogenesis under hypoxia. Nature
950 *481*, 380–384.

951 Mizuno, S., Bogaard, H.J., Voelkel, N.F., Umeda, Y., Kadowaki, M., Ameshima, S., Miyamori, I., and Ishizaki, T.
952 (2009). Hypoxia regulates human lung fibroblast proliferation via p53-dependent and -independent pathways.
953 Respir Res *10*, 17.

954 Murphy, T.A., and Young, J.D. (2013). ETA: Robust software for determination of cell specific rates from
955 extracellular time courses. Biotechnol Bioeng *110*, 1748–1758.

956 Murphy, T.A., Dang, C.V., and Young, J.D. (2013). Isotopically nonstationary 13C flux analysis of myc-induced
957 metabolic reprogramming in b-cells. Metab Eng *15*, 206–217.

958 Oldham, W.M., Clish, C.B., Yang, Y., and Loscalzo, J. (2015). Hypoxia-mediated increases in l-2-hydroxyglutarate
959 coordinate the metabolic response to reductive stress. Cell Metab *22*, 291–303.

960 Pelletier, J., Bellot, G., Gounon, P., Lacas-Gervais, S., Pouyssegur, J., and Mazure, N.M. (2012). Glycogen
961 synthesis is induced in hypoxia by the hypoxia-inducible factor and promotes cancer cell survival. Front Oncol *2*,
962 18.

963 Pescador, N., Villar, D., Cifuentes, D., Garcia-Rocha, M., Ortiz-Barahona, A., Vazquez, S., Ordonez, A., Cuevas, Y.,
964 Saez-Morales, D., Garcia-Bermejo, M.L., et al. (2010). Hypoxia promotes glycogen accumulation through hypoxia
965 inducible factor (HIF)-mediated induction of glycogen synthase 1. PLoS One *5*, e9644.

966 Puente-Santamaria, L., Wasserman, W., and del Peso, L. (2019). TFEA.ChIP: A tool kit for transcription factor
967 binding site enrichment analysis capitalizing on ChIP-seq datasets. Bioinformatics.

968 Quek, L.E., Dietmair, S., Kromer, J.O., and Nielsen, L.K. (2010). Metabolic flux analysis in mammalian cell culture.
969 Metab Eng *12*, 161–171.

970 R Core Team (2020). R: A language and environment for statistical computing (Vienna, Austria: R Foundation for
971 Statistical Computing).

972 Rabinowitz, J.D., and Enerback, S. (2020). Lactate: The ugly duckling of energy metabolism. Nat Metab *2*, 566–
973 571.

974 Ritchie, M.E., Phipson, B., Wu, D., Hu, Y., Law, C.W., Shi, W., and Smyth, G.K. (2015). limma powers differential
975 expression analyses for RNA-sequencing and microarray studies. Nucleic Acids Research *43*, e47.

976 Scott, D.A., Richardson, A.D., Filipp, F.V., Knutzen, C.A., Chiang, G.G., Ronai, Z.A., Osterman, A.L., and Smith, J.W.
977 (2011). Comparative metabolic flux profiling of melanoma cell lines: Beyond the warburg effect. J Biol Chem *286*,
978 42626–42634.

979 Sebastian, C., and Hackermüller, J. (2020). multiGSEA: A GSEA-based pathway enrichment analysis for multi-
980 omics data. BMC Bioinformatics *21*.

981 Semenza, G.L. (2012). Hypoxia-inducible factors in physiology and medicine. Cell *148*, 399–408.

982 Sheikh, K., Forster, J., and Nielsen, L.K. (2005). Modeling hybridoma cell metabolism using a generic genome-
983 scale metabolic model of mus musculus. Biotechnol Prog *21*, 112–121.

984 Stine, Z.E., Walton, Z.E., Altman, B.J., Hsieh, A.L., and Dang, C.V. (2015). MYC, Metabolism, and Cancer. Cancer
985 Discov *5*, 1024–1039.

986 Tilton, W.M., Seaman, C., Carriero, D., and Piomelli, S. (1991). Regulation of glycolysis in the erythrocyte: Role of
987 the lactate/pyruvate and NAD/NADH ratios. J Lab Clin Med *118*, 146–152.

988 Vacanti, N.M., Divakaruni, A.S., Green, C.R., Parker, S.J., Henry, R.R., Ciaraldi, T.P., Murphy, A.N., and Metallo,
989 C.M. (2014). Regulation of substrate utilization by the mitochondrial pyruvate carrier. Mol Cell *56*, 425–435.

990 Vita, M., and Henriksson, M. (2006). The Myc oncoprotein as a therapeutic target for human cancer. Semin
991 Cancer Biol *16*, 318–330.

992 Wenger, R.H., Kurtcuoglu, V., Scholz, C.C., Marti, H.H., and Hoogewijs, D. (2015). Frequently asked questions in
993 hypoxia research. Hypoxia (Auckl) *3*, 35–43.

994 Wierenga, A.T.J., Cunningham, A., Erdem, A., Lopera, N.V., Brouwers-Vos, A.Z., Pruis, M., Mulder, A.B., Gunther,
995 U.L., Martens, J.H.A., Vellenga, E., et al. (2019). HIF1/2-exerted control over glycolytic gene expression is not
996 functionally relevant for glycolysis in human leukemic stem/progenitor cells. Cancer Metab *7*, 11.

997 Wise, D.R., Ward, P.S., Shay, J.E., Cross, J.R., Gruber, J.J., Sachdeva, U.M., Platt, J.M., DeMatteo, R.G., Simon,
998 M.C., and Thompson, C.B. (2011). Hypoxia promotes isocitrate dehydrogenase-dependent carboxylation of
999 alpha-ketoglutarate to citrate to support cell growth and viability. Proc Natl Acad Sci U S A *108*, 19611–19616.

1000 Xiao, W., and Loscalzo, J. (2020). Metabolic responses to reductive stress. Antioxid Redox Signal *32*, 1330–1347.

1001 Yan, J., Goerne, T., Zelmer, A., Guzman, R., Kapfhammer, J.P., Wellmann, S., and Zhu, X. (2019). The RNA-binding
1002 protein RBM3 promotes neural stem cell (NSC) proliferation under hypoxia. Front Cell Dev Biol *7*, 288.

1003 Young, J.D. (2014). INCA: A computational platform for isotopically non-stationary metabolic flux analysis.
1004 Bioinformatics *30*, 1333–1335.

1005 Zamorano, F., Wouwer, A.V., and Bastin, G. (2010). A detailed metabolic flux analysis of an underdetermined
1006 network of CHO cells. J Biotechnol *150*, 497–508.

1007 Zhang, H., Gao, P., Fukuda, R., Kumar, G., Krishnamachary, B., Zeller, K.I., Dang, C.V., and Semenza, G.L. (2007).
1008 HIF-1 Inhibits Mitochondrial Biogenesis and Cellular Respiration in VHL-Deficient Renal Cell Carcinoma by
1009 Repression of C-MYC Activity. Cancer Cell *11*, 407–420.

1010 Zhang, H., Bosch-Marce, M., Shimoda, L.A., Tan, Y.S., Baek, J.H., Wesley, J.B., Gonzalez, F.J., and Semenza, G.L.
1011 (2008). Mitochondrial autophagy is an HIF-1-dependent adaptive metabolic response to hypoxia. J Biol Chem
1012 *283*, 10892–10903.

1013 Zhang, J., Sattler, M., Tonon, G., Grabher, C., Lababidi, S., Zimmerhackl, A., Raab, M.S., Vallet, S., Zhou, Y.,
1014 Cartron, M.-A., et al. (2009). Targeting angiogenesis via a c-Myc/hypoxia-inducible factor-1alpha-dependent
1015 pathway in multiple myeloma. Cancer Res *69*, 5082–5090.